Lawrence Radiation Laboratory
UNIVERSITY OF CALIFORNIA
LIVERMORE

UCRL-50460

THIRD PROGRESS REPORT OF LIGHT ARMOR PROGRAM

Mark L. Wilkins

July 9, 1968

Foreword

The work reported here is a continuation of the program initiated by the Advanced Research Projects Agency (ARPA) and is described in the first and second progress reports.[1,2]

The work of the following personnel of the Lawrence Radiation Laboratory is acknowledged. C. A. Honodel conducted the ballistic experiments. D. E. Giroux programmed the Hemp code. W. H. Gust made the Hugoniot measurements on the ceramics. C. F. Cline, D. R. Sawle, and K. E. Froeschner made valuable contributions to the research program. Also acknowledged are the mechanical engineering support of H. J. Rien and K. G. Hoge, and the electronic engineering support of W. L. Skinner.

Contents

FOREWORD ii

ABSTRACT 1

INTRODUCTION 1

CALCULATIONAL WORK 2

Calculation of Brittle Fracture 2

Calculation of Impact of Sharp Projectile with Ceramic Backed by Aluminum 4

IMPACT EXPERIMENTS OF SHARP PROJECTILES STRIKING CERAMIC BACKED BY ALUMINUM OR FIBER GLASS 10

BALLISTIC LIMIT EXPERIMENTS 17

Ballistic Limit Experiments with Ceramic Backed by Aluminum . . . 17

Ballistic Limit Experiments with Ceramic Backed by Woven Roving Fiber Glass 20

BACKUP PLATE STUDIES 24

ROLE OF BOND BETWEEN CERAMIC AND BACKUP PLATE 26

TENSION STRENGTHENING OF CERAMIC 26

REFERENCES 27

APPENDIX A. Derivation of Equation of State from Hugoniot Elastic Limit Experiments 28

APPENDIX B. Dynamic Testing Procedure for Screening New Composite Materials 36

APPENDIX C. Tension Test 42

Illustrations

Figure

1. Calculation of development of fracture conoid and axial crack in alumina.
2. Calculation of effect of using two layers of alumina compared to one (as in Fig. 1).
3a. Calculated penetration of aluminum target faced with ceramic (Al_2O_3) by a sharp steel projectile. Note: included in calculation are boundary conditions that correspond to 4-in. diam ring mount support for the aluminum.
3b. Cross section of calculation shown in Fig. 3a. Lines in Al above show direction of maximum principal stress; lines in Al_2O_3 above show position of fracture conoid.
4. Stress profile along axis for calculations shown in Fig. 3 at t = 0.75 μsec.
5. Stress in axial direction, σ_x, in aluminum plate at ceramic interface for calculation shown in Fig. 3.
6. Energy vs time for projectile and target from calculations shown in Fig. 3.
7. Flash radiographs of impact below ballistic limit for aluminum-backed Al_2O_3 target (projectile velocity = 2800 ft/sec; ballistic limit = 2850 ft/sec).
8. Flash radiographs of impact below ballistic limit for woven roving Al_2O_3 target backed with fiber glass (projectile velocity = 2550 ft/sec; ballistic limit = 2780 ft/sec).
9. Flash radiographs of impact above ballistic limit for aluminum-backed Al_2O_3 target projectile velocity = 3050 ft/sec; ballistic limit = 2850 ft/sec).
10. Flash radiographs of impact above ballistic limit for woven roving Al_2O_3 backed with fiber glass (projectile velocity = 2880 ft/sec; ballistic limit = 2780 ft/sec).
11. Impact below ballistic limit for target of 0.34-in. Coors AD85 alumina backed by 0.25-in. 6061-T6 aluminum.
12. Impact below ballistic limit for 0.34-in. Coors AD85 alumina backed by 0.25-in. REPCO woven roving fiber glass.
13. Experimental ballistic limits for Coors AD85 alumina bonded to 6061-T6 aluminum (30-calibre sharp projectiles).
14. Experimental data of Fig. 13 for alumina thickness greater than 0.2 in.
15. Experimental ballistic limits for Coors AD85 alumina bonded to 6061-T6 aluminum (30-calibre sharp projectiles).
16. Experimental ballistic limits for Coors AD85 alumina bonded to REPCO woven roving fiber glass (30-calibre sharp projectiles). Straight-line segments are shown linked without prejudice as to actual curve shape.
17. Experimental ballistic limits for Coors AD85 alumina bonded to REPCO woven roving fiber glass (30-calibre sharp projectiles).
18. Effect of fracture strength on time for fracture (left column: fracture strength = 3-kbar tension; right column: fracture strength = 8-kbar tension).

A1. Stress as function of one-dimensional strain.
A2. Calculated stress-spaced profile of high-explosive-induced stress wave in aluminum and boron carbide.
A3. Calculated boron carbide free surface velocity and free surface displacement as function of time.
A4. Experimental data for diamonite alumina.
A5. Experimental data for hot-pressed alumina.
A6. Experimental data for WESGO 995 alumina.

Figure

A7. Experimental data for boron carbide.

A8. Experimental data for beryllium oxide.

B1. Plate deflection test.

B2. Plate resistance to shear test.

B3. Deflection of single and laminated plates.

B4. Effect of ring mount diameter, D, on plate deflection.

B5. Effect of ram velocity on load deflection of 1/4-in. woven roving (0.6-in. diam spherical ram; 4-in. diam ring mount).

B6. Calculation of Dynapak test on aluminum (lines show direction of principal stresses; circles show positions where σ_θ stress has reached 3.5-kbar tension; line on axis is when $\sigma_{max} > 3.5$ kbar and $\gamma > 0.21$).

C1. Original geometry of rod pulled in both directions along X-axis.

C2. Calculated rod parameters using exterior measurements [Eqs. (C1), (C2) and (C3) with $L^o = 0.1$ and $r^o = 0.1$].

C3. Calculated distributions of components of total strain, ϵ_x, ϵ_r, and ϵ_θ, and corresponding stress deviators at rod midsection after elastic limit (Table CI t = 41). Stress and strain distributions are uniform below elastic limit.

C4. Calculated distributions of stresses at rod midsection after elastic limit. Note: below elastic limit stress distribution is uniform.

THIRD PROGRESS REPORT OF LIGHT ARMOR PROGRAM

Abstract

Computer calculations in conjunction with experiments are used to develop models that describe the failure of a material at the elastic limit and the subsequent failure by rupture after plastic elongation. A fracture model is developed that described the behavior of ceramic materials. The material descriptions are then used in a computer calculation of the penetration of a ceramic-faced aluminum target by a sharp steel projectile. The calculation correlates very well with a corresponding ballistic experiment that employed cameras and a flash x-ray technique to follow, in time, the various material interfaces. The important target material properties to defeat penetration and the failure modes of the materials are identified. It is noted that there is not just one material property, but a combination of properties required for an efficient armor.

An experimental method to evaluate armor candidate materials that replaces ballistic limit tests is also presented.

Introduction

In the course of a ballistic impact on a target the load on the target varies from compression to tension and to shear. No one existing material has a maximum strength for the combinations of these loads that occur. For the materials of interest in lightweight armor a high compressive strength, for example, is usually accompanied by a low tensile strength. Two-component armor allows the possibility of an armor with the best of two different strength properties. Optimization of two-component armor has been difficult because there is not only the interaction of the target and the projectile but interaction between the components of the armor. A prerequisite to the development of better lightweight armor is the understanding of these interactions during the penetration process and the identification of the important material properties. It is especially important to identify the conditions for failure of the materials. With this information material design criteria can be established. It is thought that a better armor will result if some of the weak properties of armor materials are improved even at the expense of a

strong feature of the material. Thus one of the objectives in armor research should be to look for the possibility of a tradeoff in material properties.

The application of materials to light armor is unusual because the material properties are utilized in the region of material failure; i.e., if the armor doesn't fail for a given ballistic threat it could be made lighter. In penetration of ceramic-faced armor there are several competing material failure processes that lead to an ultimate failure of the armor. The work reported here uses computer calculations to follow the penetration processes step by step. The calculations are not used to replace experiments but rather to check the understanding of experiments and to determine the important physical processes. A particular phenomenon can then be studied separately with calculations to determine the sensitivity of a process to physical parameters.

Calculational Work

Calculation of Brittle Fracture

A first requirement for the calculational work is a model to describe the observed fracture of ceramics. The brittle fracture model developed for the two-dimensional Hemp code incorporates the following assumptions:

1. Fracture is initiated on surfaces.
2. The following is the criterion for fracture: a principal stress in the plane of motion greater than 3-kbar tension.
3. There is a time delay for the complete fracture of a zone.
4. A zone that has fractured becomes the source of fracture for a nearby zone.
5. A zone can fracture only when it is within a distance $d = V_c \times \Delta t$ of a zone that has already fractured. Here V_c is the crack velocity and Δt the elapsed time after fracture of the source zone.
6. The fracture of a zone is accomplished by relaxing the strength of material to zero.

Figure 1 shows a calculation of a projectile impact with a target composed of a ceramic backed by aluminum. The ceramic is described in the compression state by an equation of state derived from Hugoniot elastic limit experiments (Appendix A) and the above fracture model for tension states. It is seen that a fracture conoid develops at the impact surface and spreads to the interface between the ceramic and the aluminum backup plate. This conoid corresponds very well to the conoids seen in flash x-ray experiments (second progress report[2]) and from recovered targets. It is seen that slightly after impact a crack is initiated on the axis opposite the impact side of the ceramic. Microscopic examination of ceramics fractured experimentally show that the calculation reproduced the actual time sequence of events.

The effect of the conoid is to limit the amount of ceramic that participates in transmitting the load to the backup plate. The highest stress level on the backup plate occurs at the center of impact, and

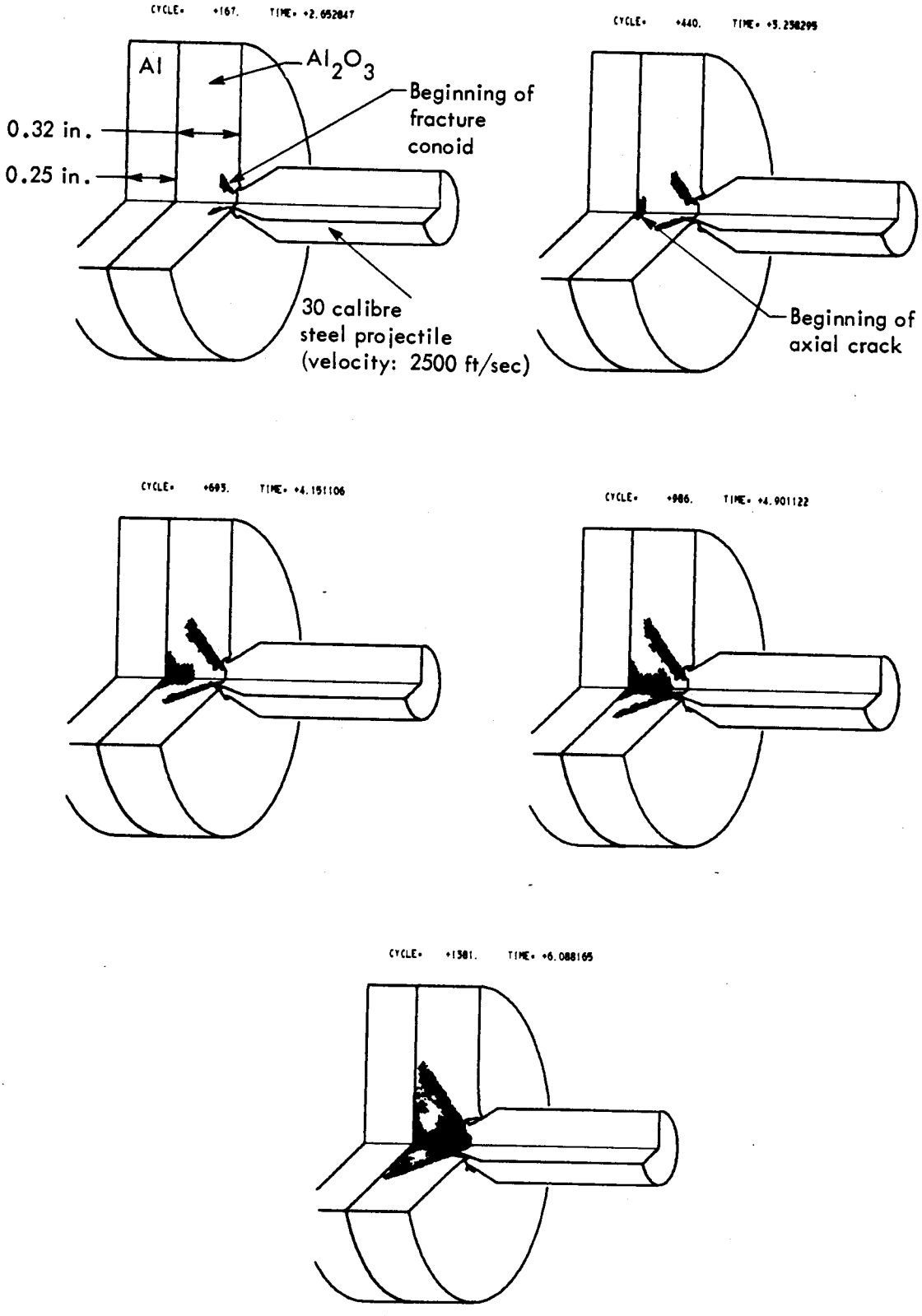

Fig. 1. Calculation of development of fracture conoid and axial crack in alumina.

it is here that the greatest compression occurs in the backup plate. The compression in the aluminum relaxes the support to the ceramic, and the stress in the ceramic becomes tensile. The axial crack that is initiated proceeds back toward the projectile (Fig. 1). The subsequent action is a general breaking up of the ceramic within the conoid from the coalescence of the cracks. The rate of the breaking up for a given ceramic depends on how well it is supported by the backup plate since the support governs the tension states in the ceramics. As the ceramic breaks up, the load to the backup plate is transmitted over smaller and smaller areas. A point is eventually reached in the breakup of the ceramic where the load on the backup plate is transmitted over a diameter corresponding roughly to the projectile diameter.

Experiments with ceramics made of two layers show lower ballistic limits than for a single ceramic layer of the same total thickness. In Table I it is seen that the ballistic limit for sharp projectiles is 250 ft/sec lower when two pieces of AD85 are used than the limit when a single piece is used. The ballistic limit for two ceramic pieces bonded together with a polyurethane adhesive is even lower. In all cases the ceramic is bonded to the aluminum.

Table I. Ballistic limits for targets of Coors AD85 alumina backed by 0.25-in. 6061-T6 aluminum.

	Ballistic limits (ft/sec)		
	Two pieces of AD85 0.16 in. thick		Single piece of AD85 0.32 in. thick
Projectile	unbonded	bonded	
Sharp cylinder	2400 ± 50	2300 ± 50	2650 ± 50

The explanation is given by the calculation shown in Fig. 2. It is seen that when two pieces of ceramic are used an axial crack forms shortly after impact at the interface between the two pieces of ceramic. This action permits the ceramic to break up sooner than it would otherwise. Hence, the effectiveness of one-half the ceramic is compromised early in the penetration process with a corresponding drop in the ballistic limit. The introduction of the adhesive between the two ceramic layers (Table I) allows an additional tension mode to develop in the ceramic from the motion of the ceramic into the adhesive since the adhesive is more compressible than the ceramic. It would thus be expected that the ballistic limit would be lower than with no adhesive.

Experiments have shown that the ceramic fracture conoids are relatively independent of impact velocity (second progress report[2]). Since the same conoids always occur over the impact velocity range-of-interest a simplification is possible when the object of a calculation is to study the load time history on a backup plate. For problems of this type the overall effect of the propagation of cracks can be simulated by:

1. Introducing the conoid into the problem at a time after impact
2. Assuming all of the material inside the conoid breaks after a certain time and introducing a new equation of state for broken ceramic.

Calculation of Impact of Sharp Projectile with Ceramic Backed by Aluminum

Figure 3 shows an impact calculation that uses the above procedure where the time scale for steps (1) and (2) were taken

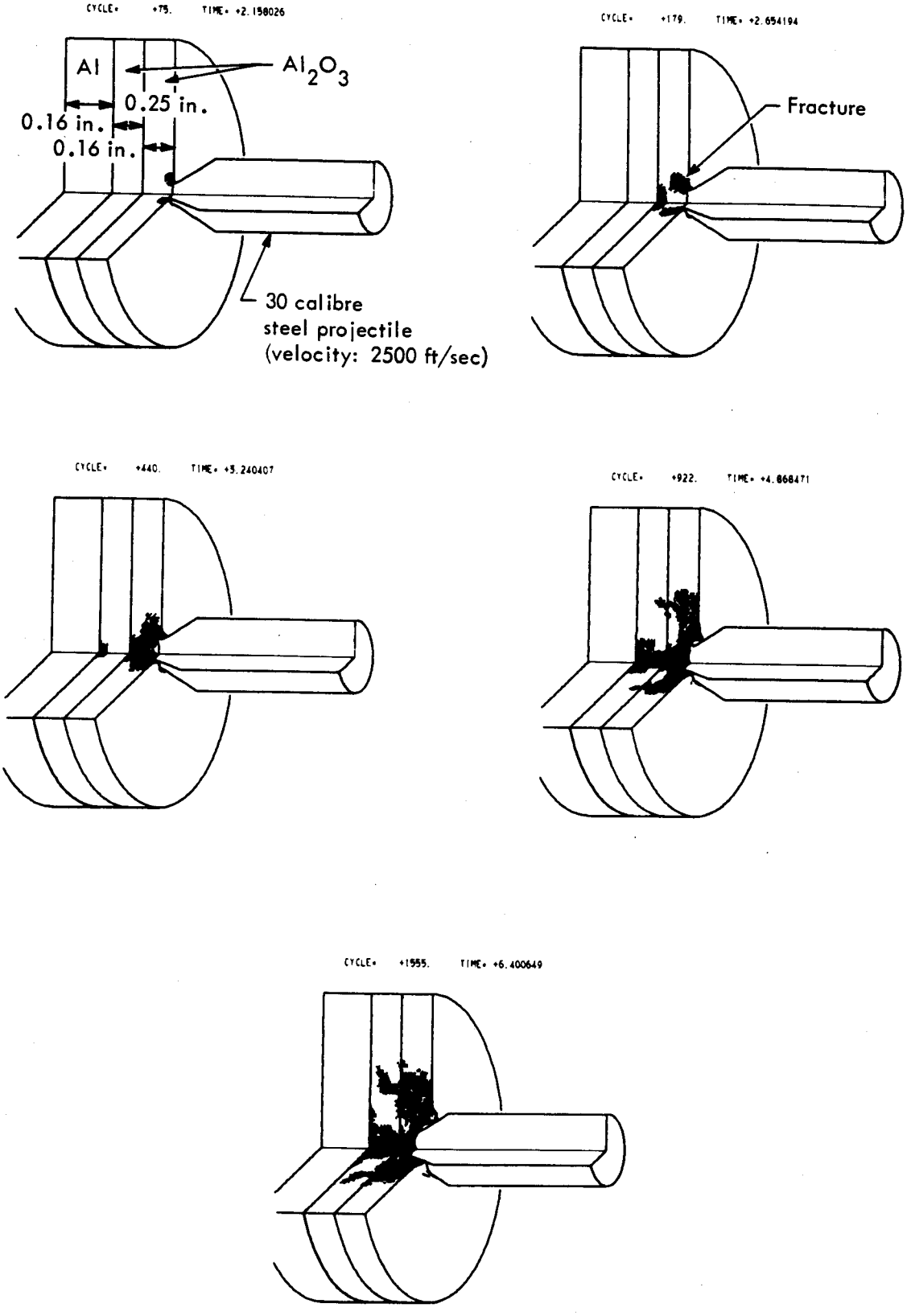

Fig. 2. Calculation of effect of using two layers of alumina compared to one (as in Fig. 1).

from Fig. 1. The equation of state of the ceramic in compression was obtained from the Hugoniot elastic limit experiments (Appendix A). The equation of state for broken ceramic was estimated by matching a computer calculation to an experiment where a steel cylinder was decelerated by broken ceramic (sequential flash x rays gave the time-position history of the cylinder; the equation of state in the calculation was adjusted to give the same history for the cylinder).

The impact velocity for the calculation (Fig. 3) is just below the ballistic limit for this target (2800 ft/sec; ballistic limit V_{BL} = 2850 ft/sec). It is seen in Fig. 3 that at ~9 μsec the tip of the projectile has been completely destroyed. The large deformation of the tip of the projectile increases the internal energy of the projectile material to the point where the strength of the material is reduced. This is accomplished in the calculation by making the strength, Y^{O}, a function of the

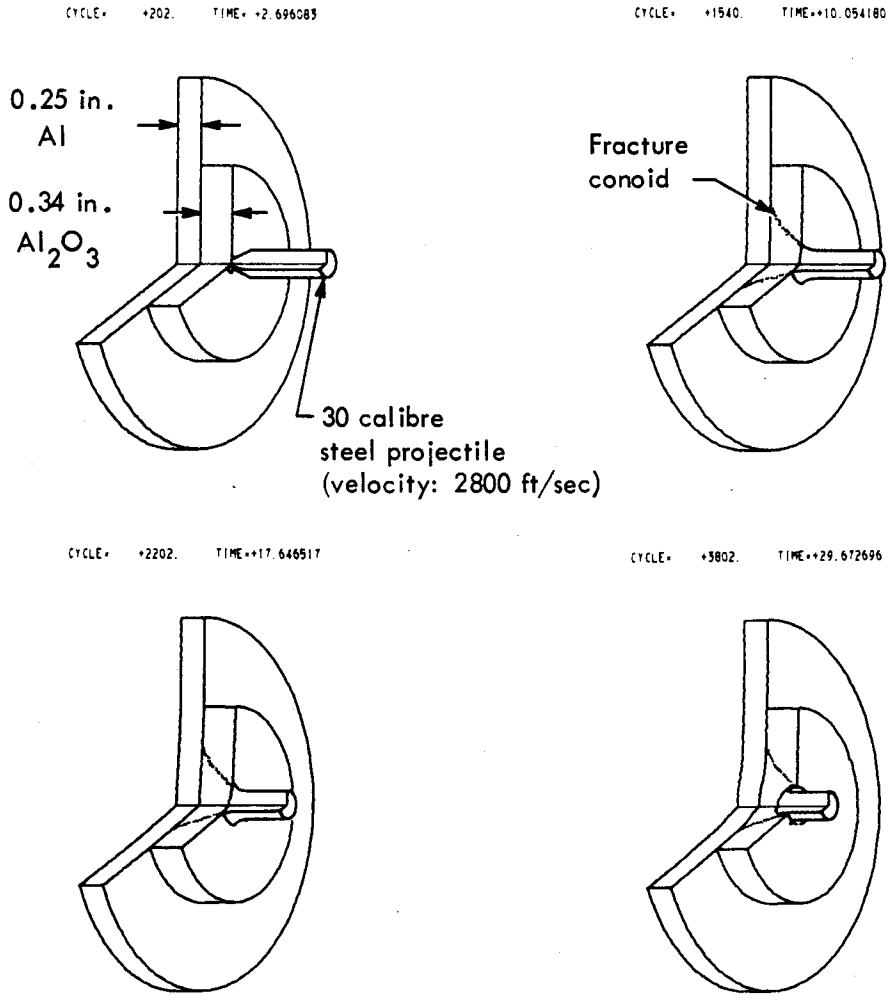

Fig. 3a. Calculated penetration of aluminum target faced with ceramic (Al_2O_3) by a sharp steel projectile. Note: included in calculation are boundary conditions that correspond to 4-in. diam ring mount support for the aluminum.

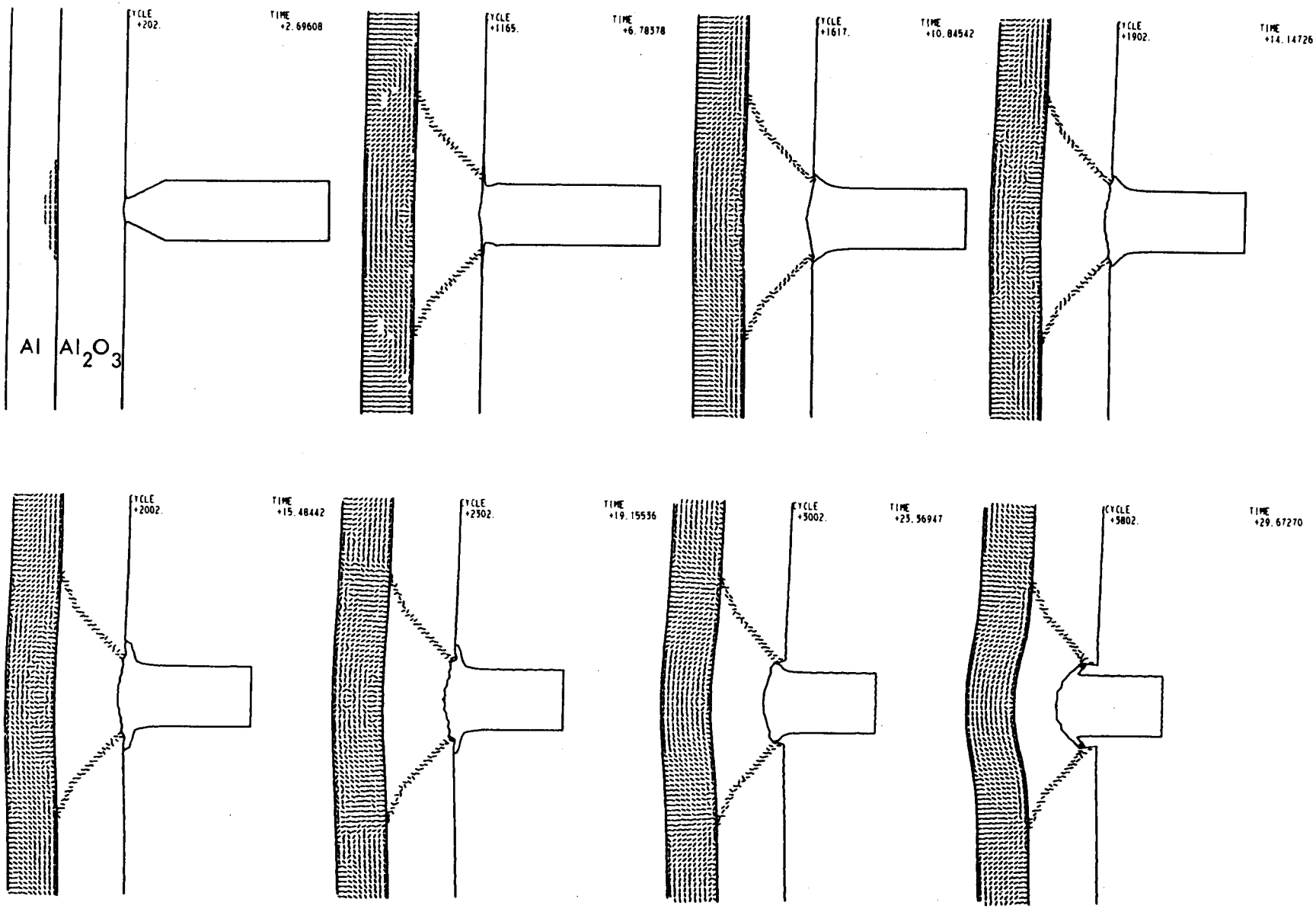

Fig. 3b. Cross section of calculation shown in Fig. 3a. Lines in Al above show direction of maximum principal stress; lines in Al_2O_3 above show position of fracture conoid.

internal energy. Figure 4 shows the stress in the direction of motion σ_x, for positions along the axis. The figure shows the stress at 0.75 μsec after impact, but the same general position and magnitude persists for about 10 μsec. The load on the target can be thought of as a steady-state load for this period of time. In Fig. 5, the stress in the axial direction, σ_x, is shown as a function of radius for a position just inside the aluminum backup plate at the ceramic interface. It is seen that the stress level is between 4 and 10 kbar. After 10 μsec the entire central portion of the aluminum plate is moving at a velocity of 0.015 cm/μsec. This is

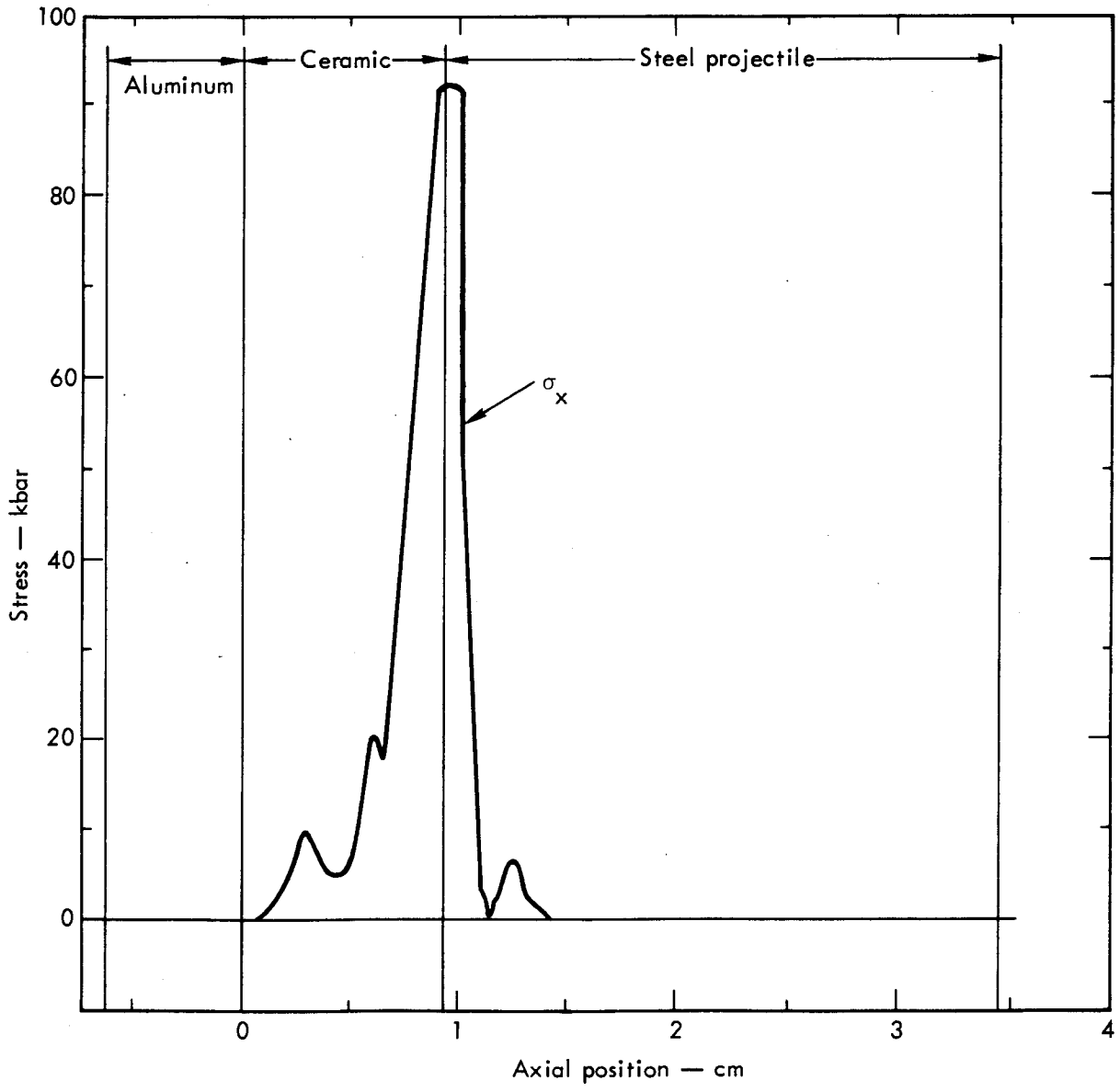

Fig. 4. Stress profile along axis for calculations shown in Fig. 3 at t = 0.75 μsec.

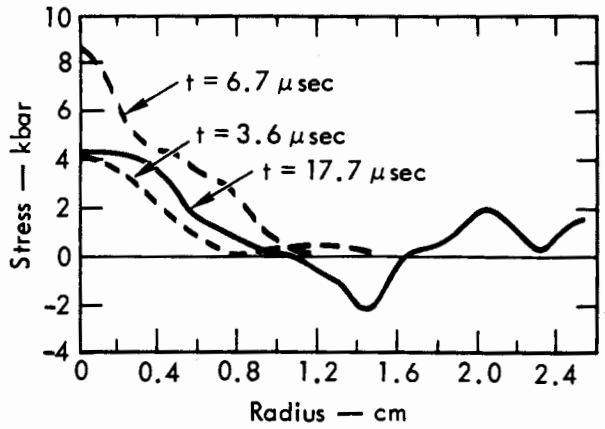

Fig. 5. Stress in axial direction, σ_x, in aluminum plate at ceramic interface for calculation shown in Fig. 3.

exactly the velocity recorded by a streak camera of the corresponding experiment (see next section).

A better understanding of the sequence of events can be obtained with the aid of Fig. 6. This figure shows the calculated projectile kinetic energy and the total target energy as a function of time. With reference to Fig. 6 and Fig. 3:

1. From 0 to 9 μsec the projectile tip is being destroyed. The rate of projectile energy loss increases as the surface area of the projectile in contact with the target increases.

2. At 9 μsec the tip has been completely destroyed. The tip represents ~10% of the projectile mass. The full cylinder cross section is now in contact with the target.

3. From 9 to 15 μsec the rate of projectile energy loss is high chiefly due to the loss of projectile mass. It is seen that the increase in the target energy is considerably less than the projectile energy lost.

4. After 15 μsec the erosion of the projectile stops, and the rate of projectile energy lost is equal to the rate of gain in energy of the target. As time progresses the crushing of the ceramic allows the load on the backup plate to be concentrated over smaller areas until it is eventually concentrated over an area corresponding to the projectile diameter.

The positions as a function of time for the various interfaces in the calculation correlate very well with the corresponding experiment described in the next section. This implies that the load-time history on the backup plate is correct. Some of the main results of the calculation are:

1. The 40-kbar compressive yield strength of the ceramic is sufficient to destroy the tip of the projectile.

2. There is a rapid loss in projectile energy ~10 μsec after impact.

3. The target absorbs only approximately 60% of the projectile energy; the remainder is carried off by deflected

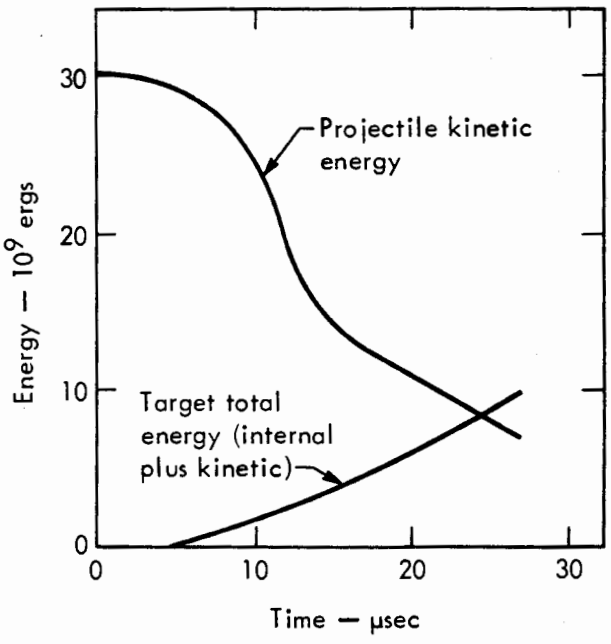

Fig. 6. Energy vs time for projectile and target from calculations shown in Fig. 3.

projectile material. The large fraction of energy carried off by deflected projectile material was noted in experiments by J. Taylor.[3]

Impact Experiments of Sharp Projectiles Striking Ceramic Backed by Aluminum or Fiber Glass

Flash x rays (600 kV; 2×10^{-8} sec exposure time) were used to study the impact of sharp projectiles on Coors AD85 alumina backed by either 6061-T6 aluminum or REPCO woven roving fiber glass. The impact velocities were chosen below and above the ballistic limits for the two targets. The objectives of the experiments were:

1. To determine whether a difference in loading history could be detected for aluminum and fiber glass backup plates
2. To obtain position-vs-time data of the various interfaces and correlate them with calculations on the Hemp code

The front and rear surface of the projectile and the rear surface of the target can be easily seen with the x rays. However, the ceramic backup plate interface at the center of impact ordinarily cannot be seen due to a lack of contrast. Therefore a gold strip 5 mils thick and 60 mils wide was laid along the center of the targets on the ceramic backup plate interface. In this manner all of the interface of the projectile and target materials could be readily followed in time with sequential shots of the flash x rays. The results are shown in Figs. 7 through 10. The x-ray heads are placed around the target axis. An image of the true length of the foil is obtained only for the x-ray head perpendicular to the foil length. For the other heads the length of the foil appears shorter than the true length.

The discrete x-ray shots were keyed to streak camera records that continuously followed in time the positions of the projectile rear surface and the target rear surface. The resulting position-vs-time plots from the x-ray and camera data are shown in Figs. 11 and 12. It is seen that the erosion process transforms the projectile from a pointed cylinder 2.81 cm in length into a blunt cylinder 1.4 cm in length. The calculation shown in Figs. 3a and 3b, predicted this result.*

Inspection of Figs. 11 and 12 shows that the ceramic resists the penetration of the projectile for a longer period of time when it is backed by aluminum than it does when it is backed by fiber glass. This result is due to the better support the aluminum offers the ceramic and hence greater time delay until the eventual breaking up of the ceramic.

It can also be detected that a fiber glass backup plate undergoes a larger deflection than an aluminum backup plate. The point

*The ballistic limit is very sensitive to the amount of projectile material that is eroded. When the mass of the projectile is reduced by 12%, the experimental ballistic limit for the target shown in Fig. 7 increases from 2850 ft/sec to 3040 ft/sec. Thus it is not surprising that there is scatter in experimental ballistic limit data.

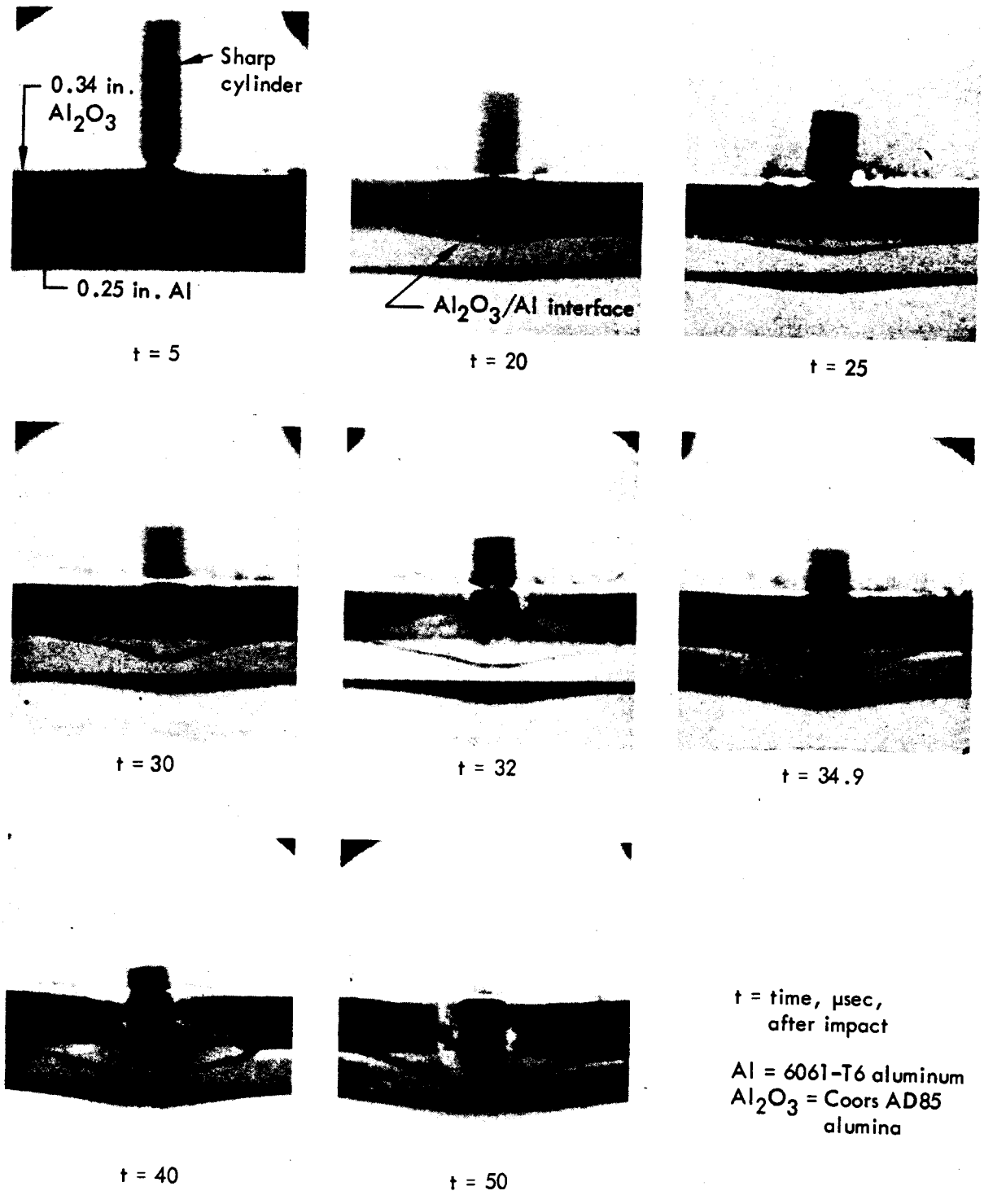

Fig. 7. Flash radiographs of impact below ballistic limit for aluminum-backed Al_2O_3 target (projectile velocity = 2800 ft/sec; ballistic limit = 2850 ft/sec).

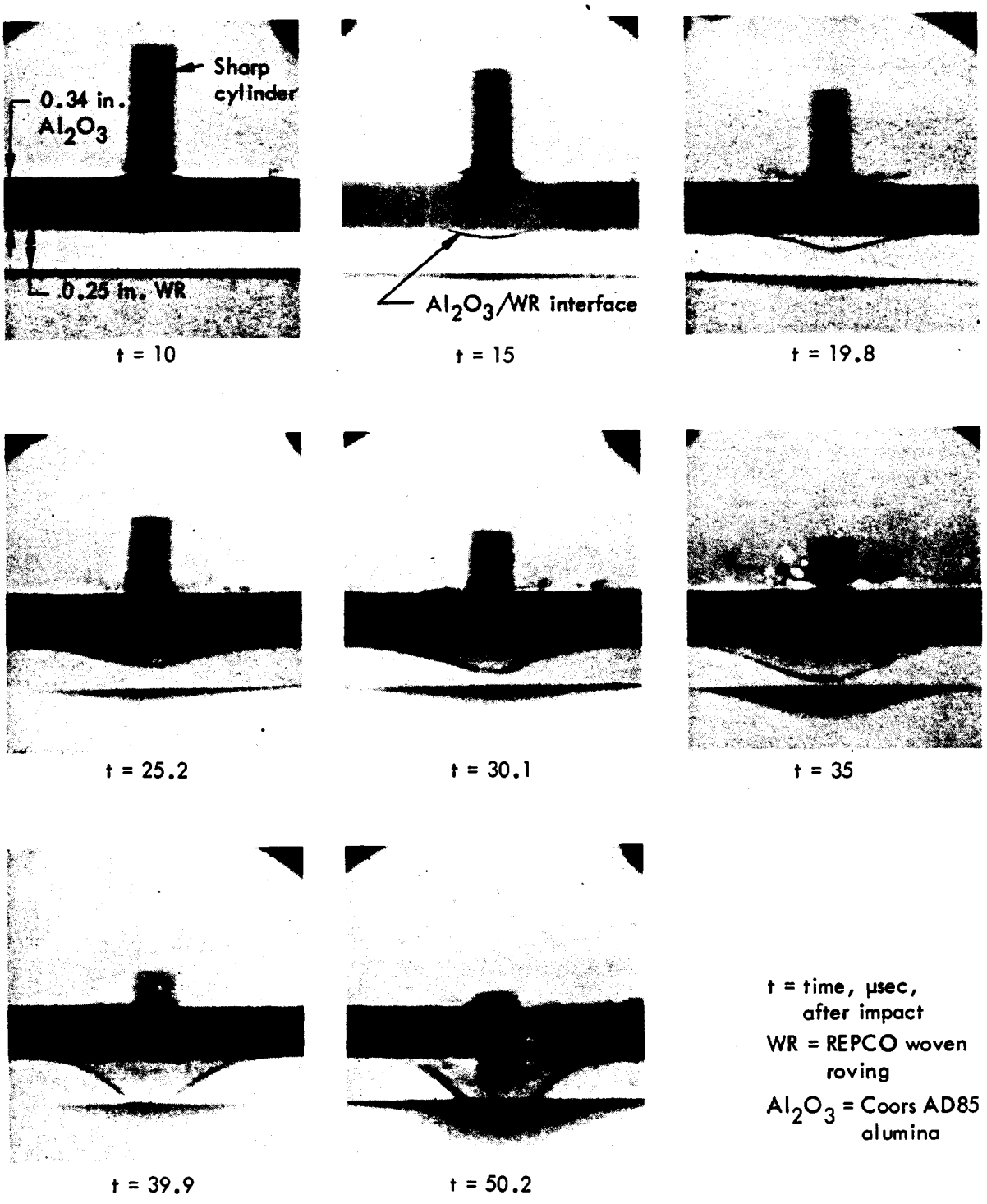

Fig. 8. Flash radiographs of impact below ballistic limit for woven roving Al_2O_3 target backed with fiber glass (projectile velocity = 2550 ft/sec; ballistic limit = 2780 ft/sec).

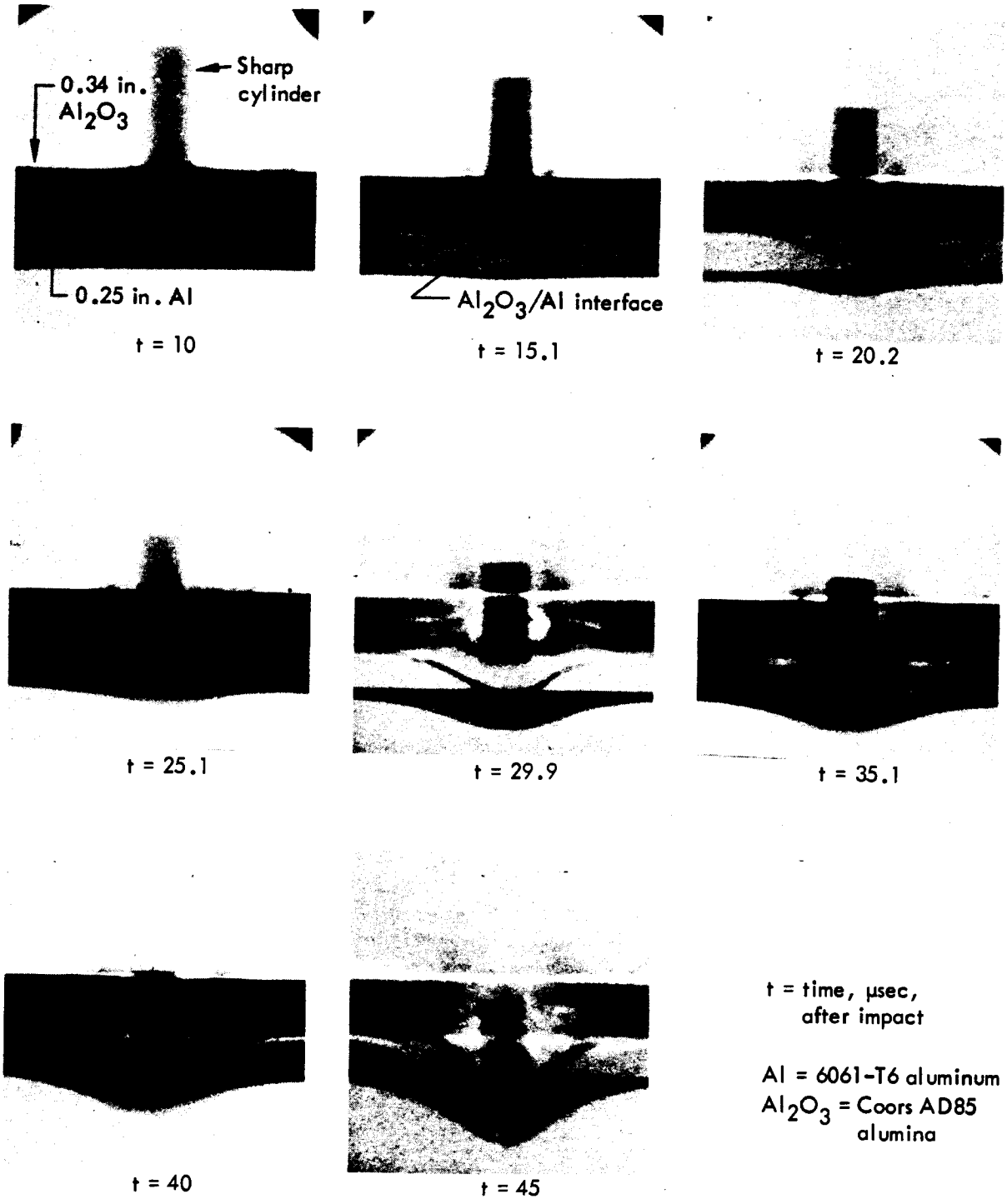

Fig. 9. Flash radiographs of impact above ballistic limit for aluminum-backed Al_2O_3 target (projectile velocity = 3050 ft/sec; ballistic limit = 2850 ft/sec).

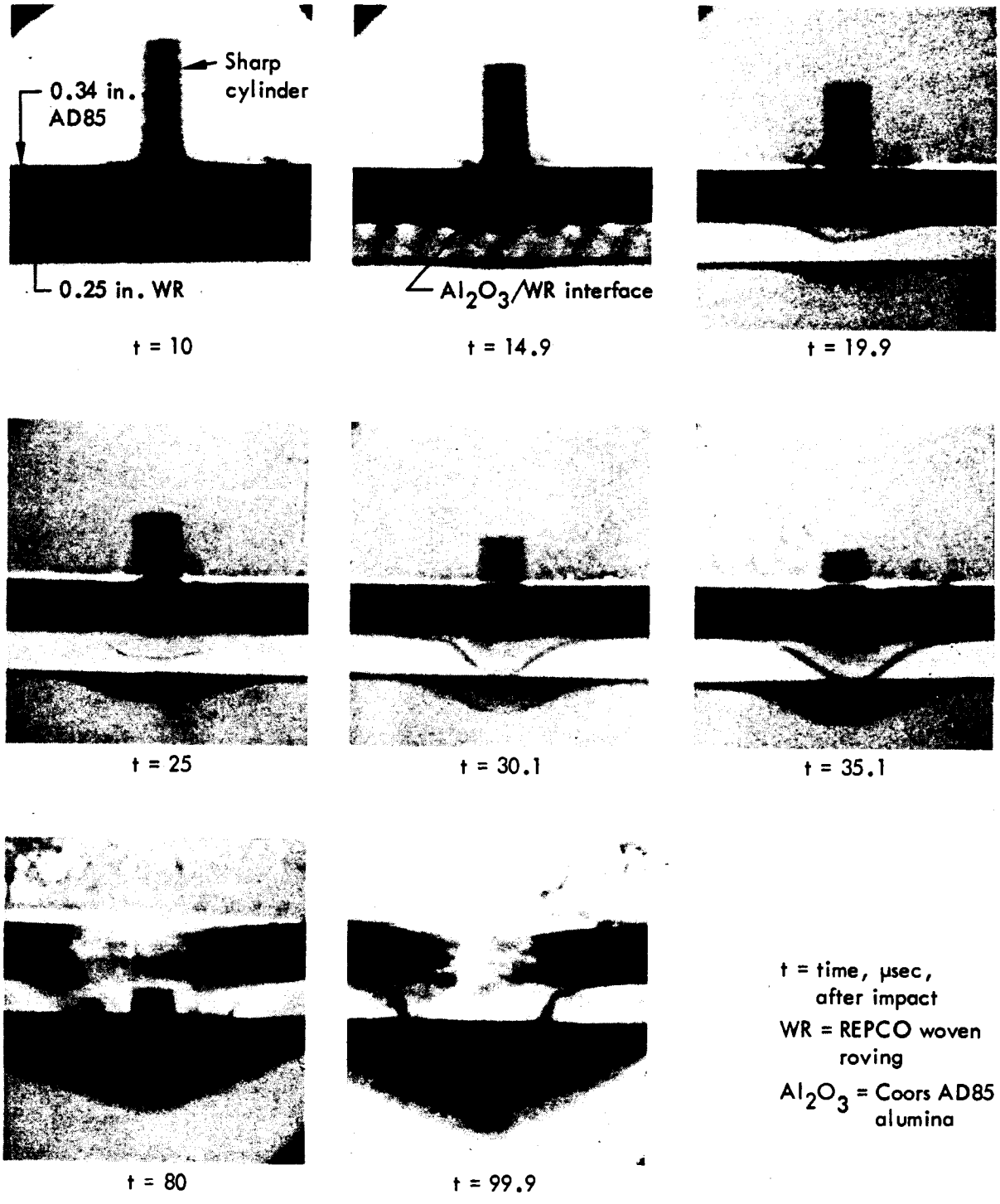

Fig. 10. Flash radiographs of impact above ballistic limit for woven roving Al_2O_3 backed with fiber glass (projectile velocity = 2880 ft/sec; ballistic limit = 2780 ft/sec).

here is that the projectile defeat mechanism for an aluminum-backed ceramic target is due mainly to the rigidity property of the aluminum plate, while the projectile defeat mechanism for the target backed with fiber glass is due mainly to the large deflection property of the fiber glass.

To demonstrate these two mechanisms the ballistic limit was determined for 0.34-in. thick tile of Coors AD85 alumina backed by:

1. 0.25-in. 6061-T6 aluminum
2. Two pieces of 0.125-in. 6061-T6 aluminum.

The effective rigidity for case 2 is thus less than that for case 1.

The corresponding ballistic limits are:

1. V_{BL} = 2850 ± 50 ft/sec (single piece of aluminum)
2. V_{BL} = 2550 ± 50 ft/sec (two pieces of aluminum)

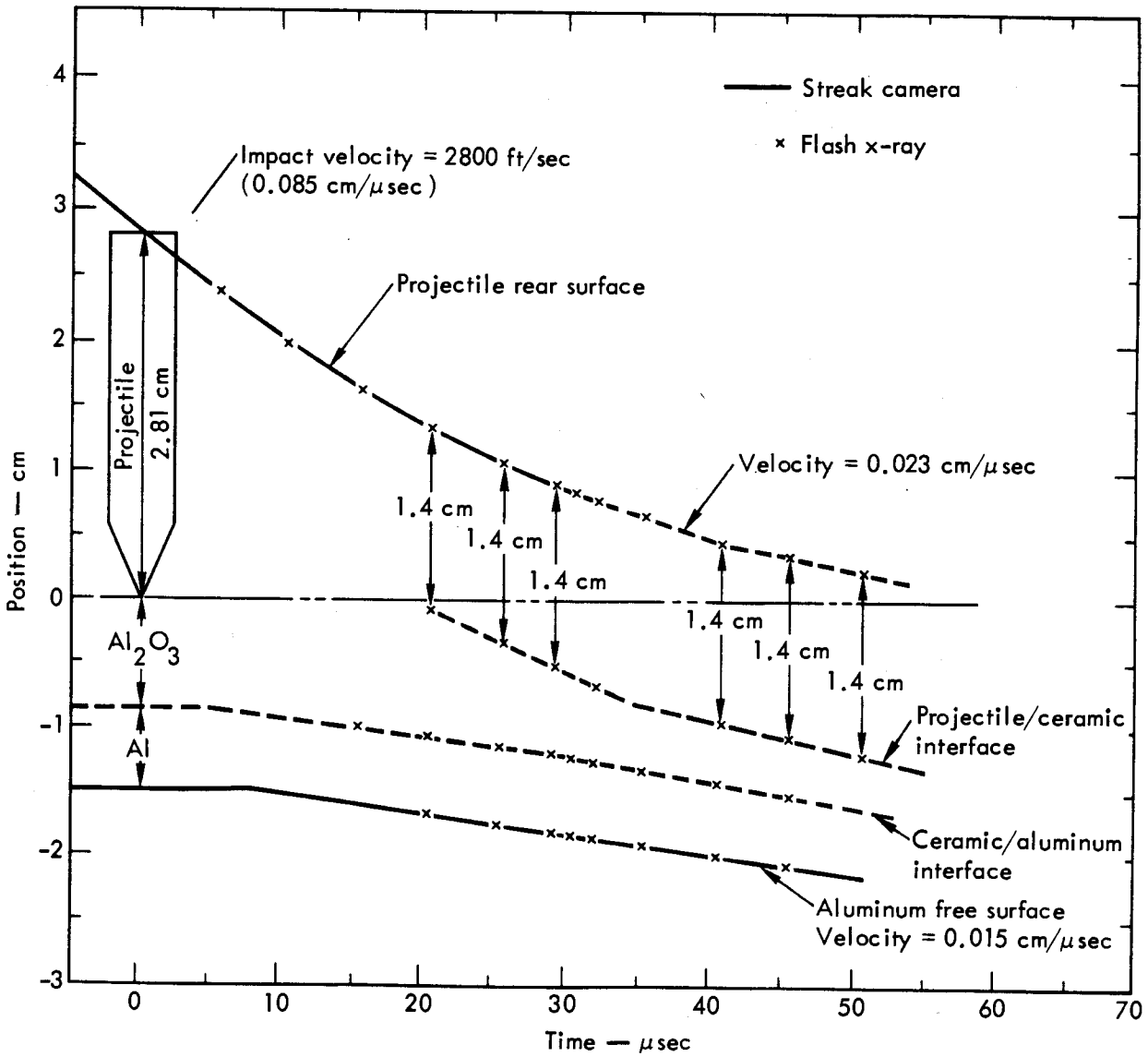

Fig. 11. Impact below ballistic limit for target of 0.34-in. Coors AD85 alumina backed by 0.25-in. 6061-T6 aluminum.

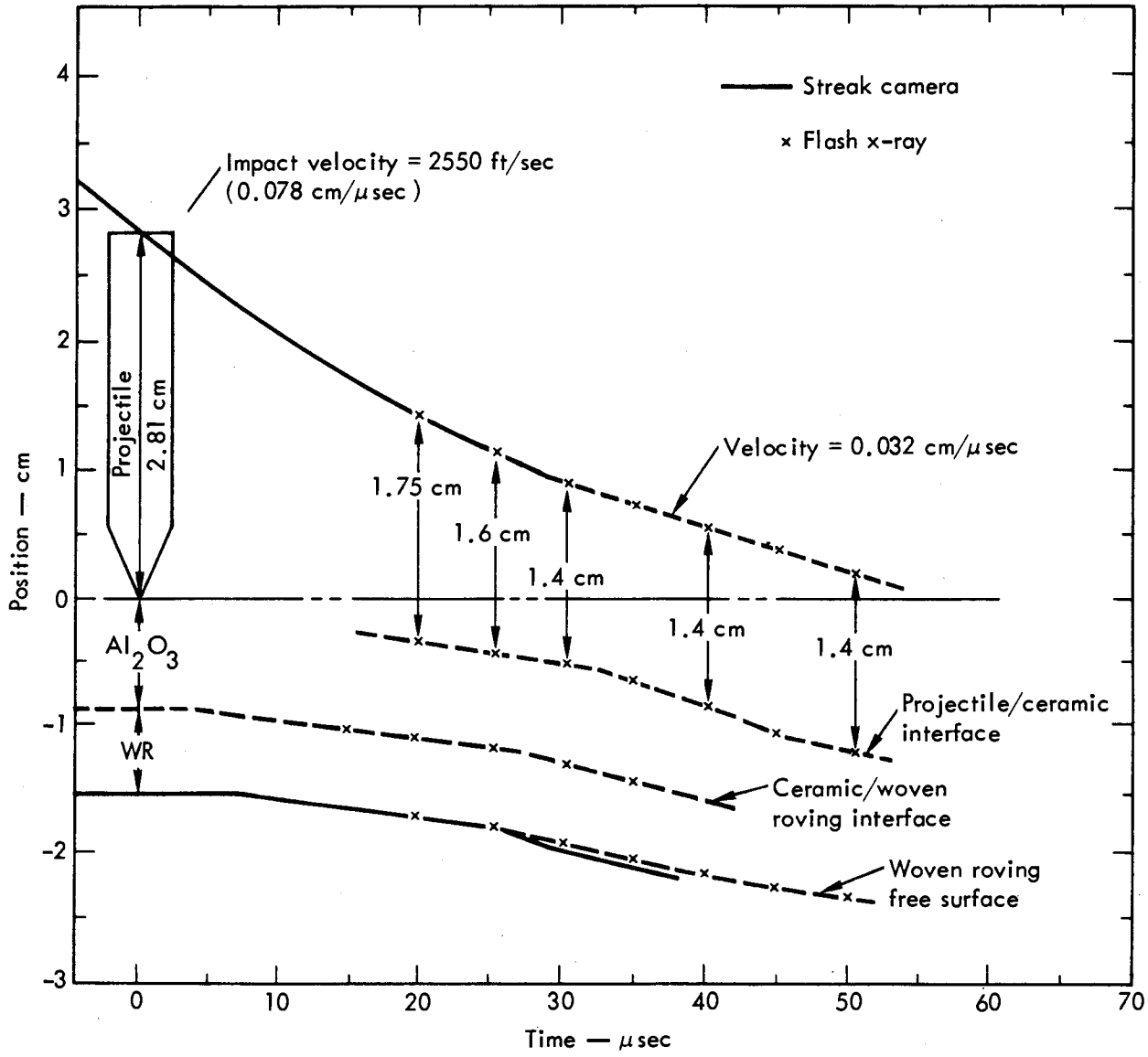

Fig. 12. Impact below ballistic limit for 0.34-in. Coors AD85 alumina backed by 0.25-in. REPCO woven roving fiber glass.

Similar experiments were performed with the ceramic backed by 0.25-in. thick REPCO woven roving fiber glass made up as:

1. One 0.25-in. thick piece
2. Two pieces 0.125 in. thick
3. One piece 0.125 in. thick plus three layers 0.048 in. thick

The corresponding ballistic limits are:

1. V_{BL} = 2780 ± 50 ft/sec (single piece of fiber glass)
2. V_{BL} = 2690 ± 50 ft/sec (two pieces of fiber glass)
3. V_{BL} = 2700 ± 50 ft/sec (multiple layers of fiber glass)

It should be noted that in these experiments there was a polyurethane adhesive between the ceramic and the first plate only.

It is seen that there is less degradation in the ballistic performance for a fiber glass backup plate made up of multiple thicknesses compared to aluminum. The reason for this is that the main projectile

defeat mechanism of the target does not depend on the stiffness property of the fiber glass. Therefore it did not make much difference when the stiffness of the backup plate was compromised by making it from multiple layers. However, for the aluminum backup plate the rigidity is the important characteristic, and the ballistic limit drops when this property is reduced.

It should be made clear that rigidity and the ability to deflect are both fundamental requirements for the backup plate. Some minimum stiffness is required for an effective fiber glass backup plate. The point here is that there exists two predominant backup plate properties that are made manifest with fiber glass and aluminum backup plates.

The role that a large deflection plays as a mechanism of defeat of a projectile by the target was examined by supporting targets by:

1. 4-in. diam ring mounts
2. 2-in. diam ring mounts

The 2-in. ring mounts limit the extent of the backup plate deflection compared to the 4-in. ring mounts. It has already been determined that a 4-in. ring mount gives the same ballistic limit data as an essentially infinite diameter mount for the targets of interest.

The ballistic limit for 0.34-in. thick tile of Coors AD85 alumina backed by 0.25-in. 6061-T6 aluminum remained about the same for the two cases (see Appendix B). The ballistic limit for a similar target backed by 0.25-in. fiber glass was:

1. V_{BL} = 2780 ± 50 ft/sec (4-in. mount)
2. V_{BL} = 2350 ± 50 ft/sec (2-in. mount)

The point here is that the aluminum backup plate does not undergo a large enough deflection to be adversely affected by a 2-in. mount aperture. The defeat mechanism for the ceramic backed with fiber glass, however, depends on a large deflection. The 2-in. mount limited the deflection, and the ballistic limit dropped.

Ballistic Limit Experiments

Ballistic Limit Experiments with Ceramic Backed by Aluminum

Figure 13 shows the experimental ballistic limits, V_{BL}, for targets of AD85 alumina bonded to 6061-T6 aluminum. It is seen that there are abrupt changes in the slopes of the curves of constant ceramic thickness when the aluminum plate thickness is ~0.23 in. Inspection of the targets revealed that the backup plate failure was by tension normal to the impact direction for plates thinner than 0.23 in. and by shear for plates thicker than 0.23 in. The tension failure started on the side opposite the impact, and the shear failure started on the impact side. The shear failure punched out aluminum plugs the diameter of the projectile from the backup plate. Referring to Fig. 13, the experimental ballistic limits for a target with a constant ceramic thickness face increases as the backup plate thickness increases due to the increased support the thicker plates give to the ceramic. However,

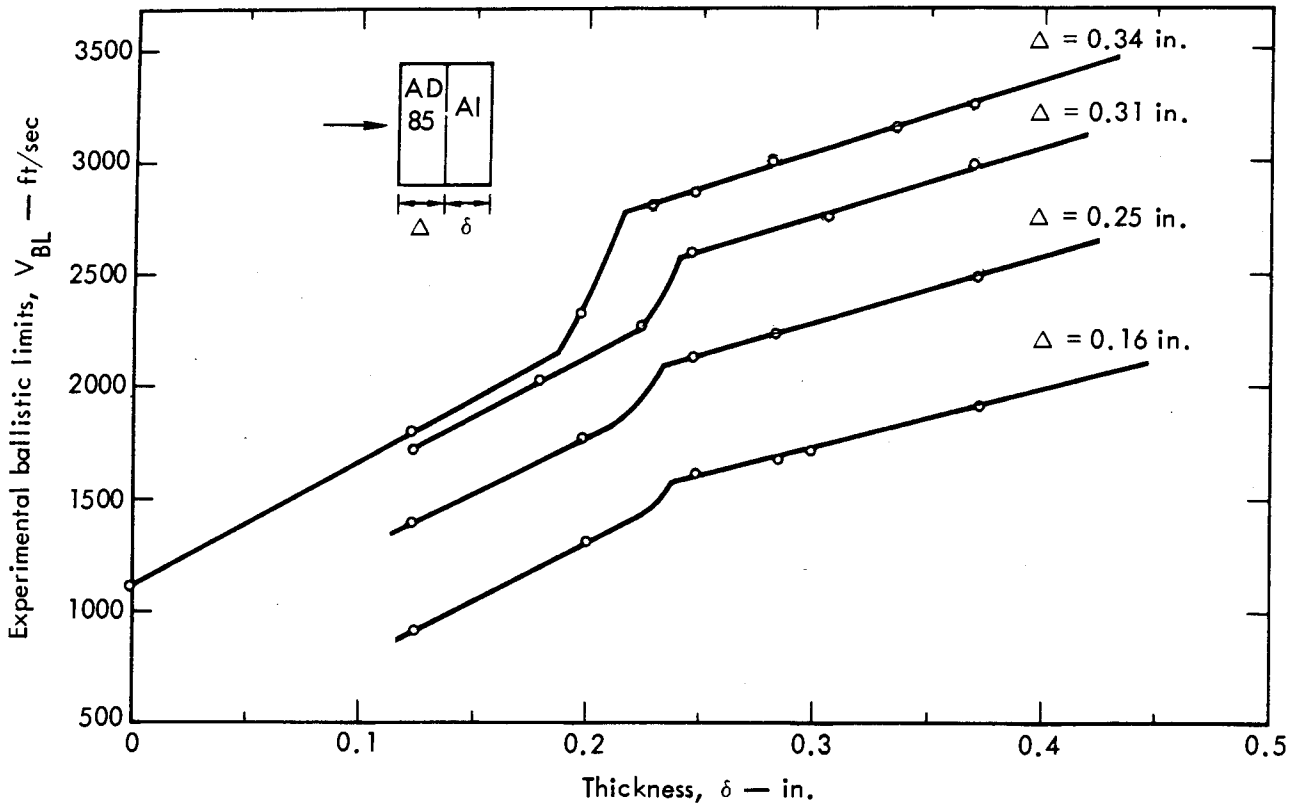

Fig. 13. Experimental ballistic limits for Coors AD85 alumina bonded to 6061-T6 aluminum (30-calibre sharp projectiles).

with increasing impact velocities the load on the aluminum increases until a stress level is reached where the aluminum undergoes compression failure at the ceramic interface with subsequent high shear forces around the rim of the loaded area. The shear forces lead to punching out a plug of aluminum. The stress level where the shear forces predominate represents the maximum support the aluminum can offer to the ceramic. The further increase in V_{BL} as more aluminum is added is related to the increase in energy required for a blunt cylinder to shear out thicker plugs of aluminum.

The stress in the ceramic is primarily elastic; therefore the magnitude of the stress varies directly with the projectile impact velocity. A reasonable assumption is that the stress at the ceramic-aluminum interface varies inversely with the ceramic thickness. Thus, the stress at the backup plate varies directly with the impact velocity and inversely with the ceramic thickness. By the above assumptions a constant ratio of impact velocity to ceramic thickness implies the same stress magnitude at the backup plate. Since it is the stress level at the backup plate that governs the behavior of the targets it might be expected that the structure of the curves shown in Fig. 13 occurs at common stress levels. Thus, the ratio of the impact velocity to the ceramic thickness should be constant for a given backup plate thickness. This was, in fact, found

to be true. All of the data in Fig. 13 fall on a single curve when the ceramic thickness is greater than 0.2 in. as shown in Fig. 14. A constant value of V_{BL}/ceramic thickness for a given backup plate thickness represents a straight line through the origin for plots of V_{BL} vs ceramic thickness (Fig. 15). However, it would not be expected that the V_{BL} curve should pass through the origin as the ceramic thickness goes to zero because the aluminum backup plate has a finite ballistic limit. Also, the penetration phenomenon changes for impact velocities below 1000 ft/sec because the projectile point is not completely destroyed for impacts below this velocity. From the data given in Fig. 13 it is estimated that the plot shown in Fig. 14 is valid for AD85 ceramic thicknesses ranging from 0.2 to 0.4 in.

In resumé, the ballistic limit for targets of a fixed ceramic thickness backed by aluminum plates increases as the aluminum is made thicker and hence stiffer. A plate thickness is finally reached where the resistance to deflection is so great that shear forces are effective in punching out the area corresponding to the diameter

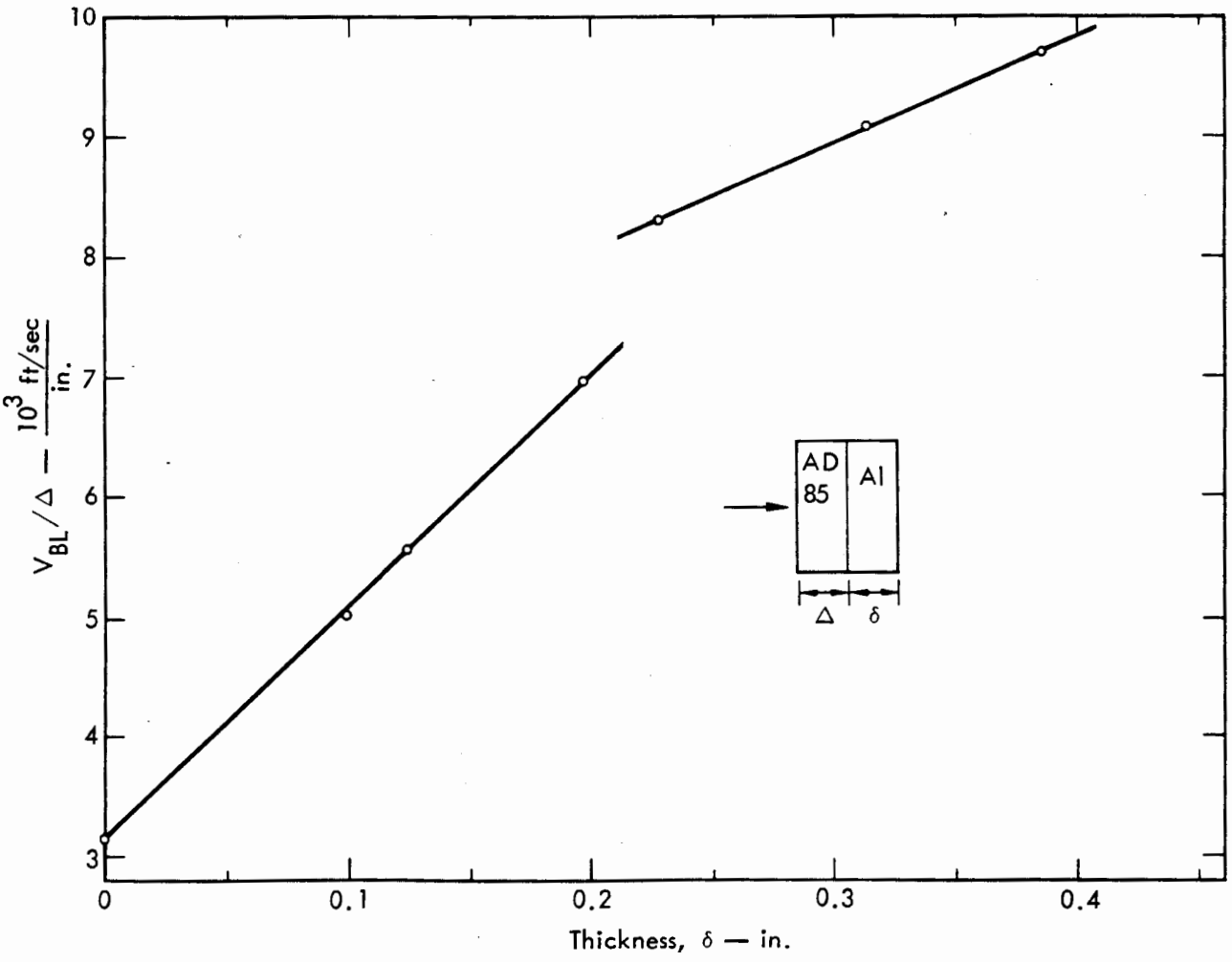

Fig. 14. Experimental data of Fig. 13 for alumina thickness greater than 0.2 in.

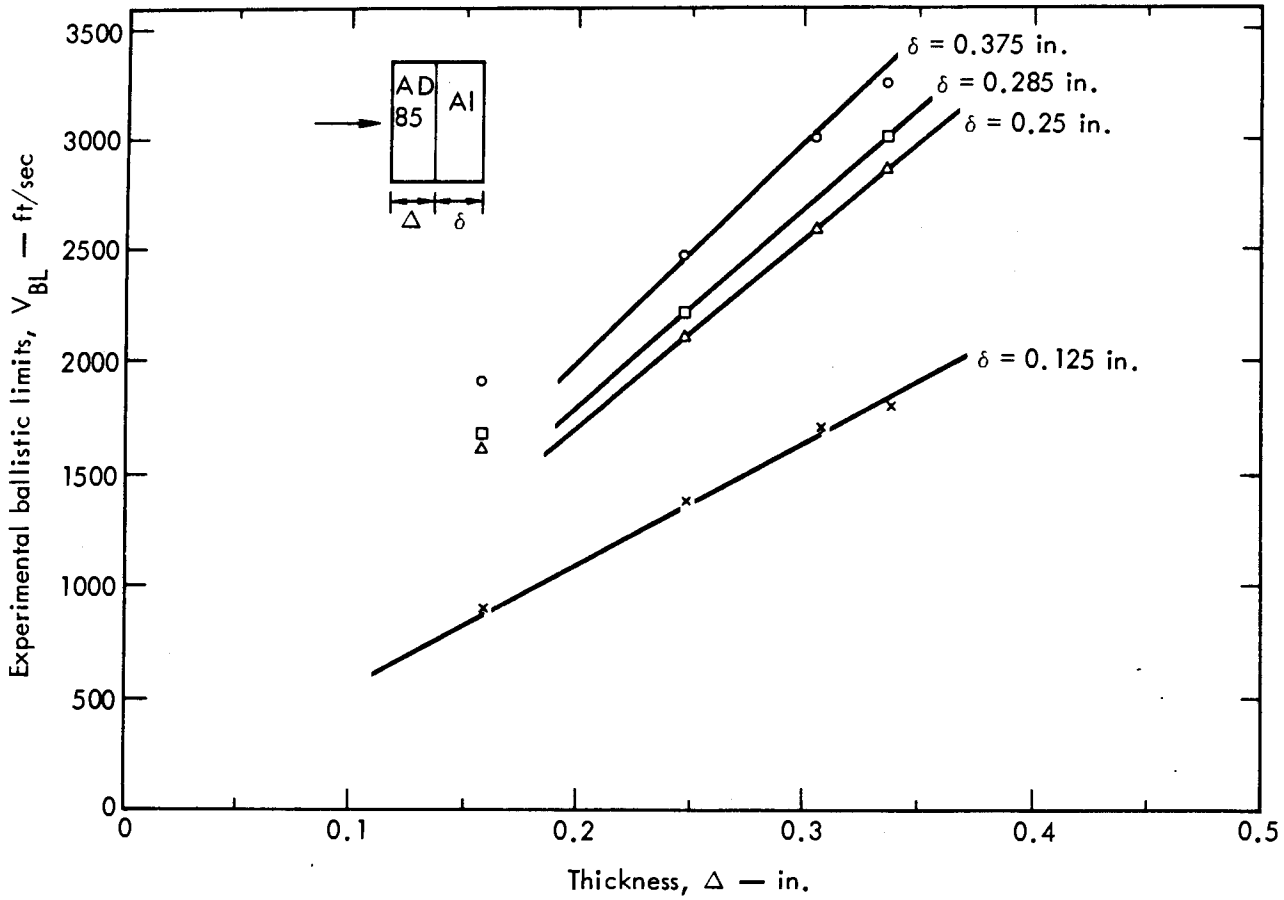

Fig. 15. Experimental ballistic limits for Coors AD85 alumina bonded to 6061-T6 aluminum (30-calibre sharp projectiles).

of the projectile. Therefore, the stiffness of the backup plate should be increased only to a value determined by the resistance of the material to compression and subsequent shear failure at the load area. For the materials discussed here this failure occurs for aluminum plates thicker than 0.23 in. The optimum target design to defeat the sharp projectile is an aluminum plate 0.23 in. thick faced with a thickness of AD85 alumina to achieve the desired ballistic limits (Fig. 13).

Ballistic Limit Experiments with Ceramic Backed by Woven Roving Fiber Glass

The ballistic limit experiments described in the preceding sections with AD85 alumina and aluminum backup plates were repeated with REPCO woven roving fiber glass backup plates. The variation in backup plate thickness was obtained by using laminates of 0.25-, 0.125-, and 0.048-in. thick woven roving. The thicker laminates were placed toward the ceramic. A polyurethane adhesive was used between the ceramic and the first fiber glass plate only. Laminates of a composite material do not necessarily reproduce the same physical characteristics that an integral piece of the same total thickness reproduces. For example, a plate with a nominal thickness of 0.25 in. made up as five pieces of 0.048-in. thick woven roving does not have the same load-deflection

properties that a plate manufactured as a single piece has.

This result would be expected since there are 12 layers of glass in a single piece of 0.25-in. woven roving and a total of 10 layers of glass in 5 pieces of 0.048-in. thick REPCO fiber glass. However, even when 6 pieces of 0.048-in. material are used to keep the same number of glass layers constant the two plates have different load-deflections characteristics. In the ballistic application an integral piece of woven roving fiber glass is superior to laminates even though the glass content is the same. The point here is that for experiments with different thicknesses of fiber glass the plate thicknesses obtained by using laminates do not necessarily belong to the same family of material as the integral pieces. However, it was found that if at least one piece of fiber glass was thick, 0.25 in. or 0.125 in., the ballistic limit data appeared to follow a consistant pattern (Figs. 16 and 17).

It is noted that the structure of the curves in Fig. 16 is very similar to the experimental results when aluminum is used as a backup plate. Examinations of targets showed a failure by compression on the ceramic side of the fiber glass over an area corresponding to the projectile diameter. The compression failure caused a shear failure and buckling of the glass fibers in the adjacent material. This backup plate failure is analogous to the shear failure described for aluminum in the preceding section. It could not be determined whether the thin fiber glass had failed by tension in a way similar to the failure of the thin aluminum plates described earlier. The V_{BL} increases at a slower rate for fiber glass thicknesses greater than 0.25 in. compared to aluminum backup plates shown in Fig. 13. The reason for this is that the resistance to shear is less for fiber glass compared to aluminum (see Fig. B2).

The similarity between the V_{BL} data for aluminum and woven roving backup plates was at first puzzling because the static properties are different. Even the value of V_{BL}/Δ corresponded to the aluminum results of fiber glass thickness on either side of the transition from low to high ballistic limits shown in Fig. 18. An explanation was obtained by dynamic load-deflection measurements (Appendix B). It was found that under the ballistic impact conditions the behavior of REPCO woven roving plates approaches that of aluminum plates. The maximum dynamic load at failure is the same for 0.25-in. plates of woven roving fiber glass and 6061-T6 aluminum. The fiber glass reached the maximum load at a larger deflection which is consistant with the ballistic results where targets backed with fiber glass require a large deflection to defeat a projectile.

With the knowledge that the good ballistic performance of woven roving fiber glass is due to dynamic properties, the problem of developing better fiber glass becomes extremely difficult. It is known that the resin must break away from the glass fibers after impact in order for the plate to undergo a large excursion. The finish on the glass fibers is very important since it influences the bond between the fibers and the resin. Thus in composites there are interactions between the fibers, the finish, and the matrix. An improvement in the compressive strength of the matrix, for example, can result in an adverse coupling effect with the finish

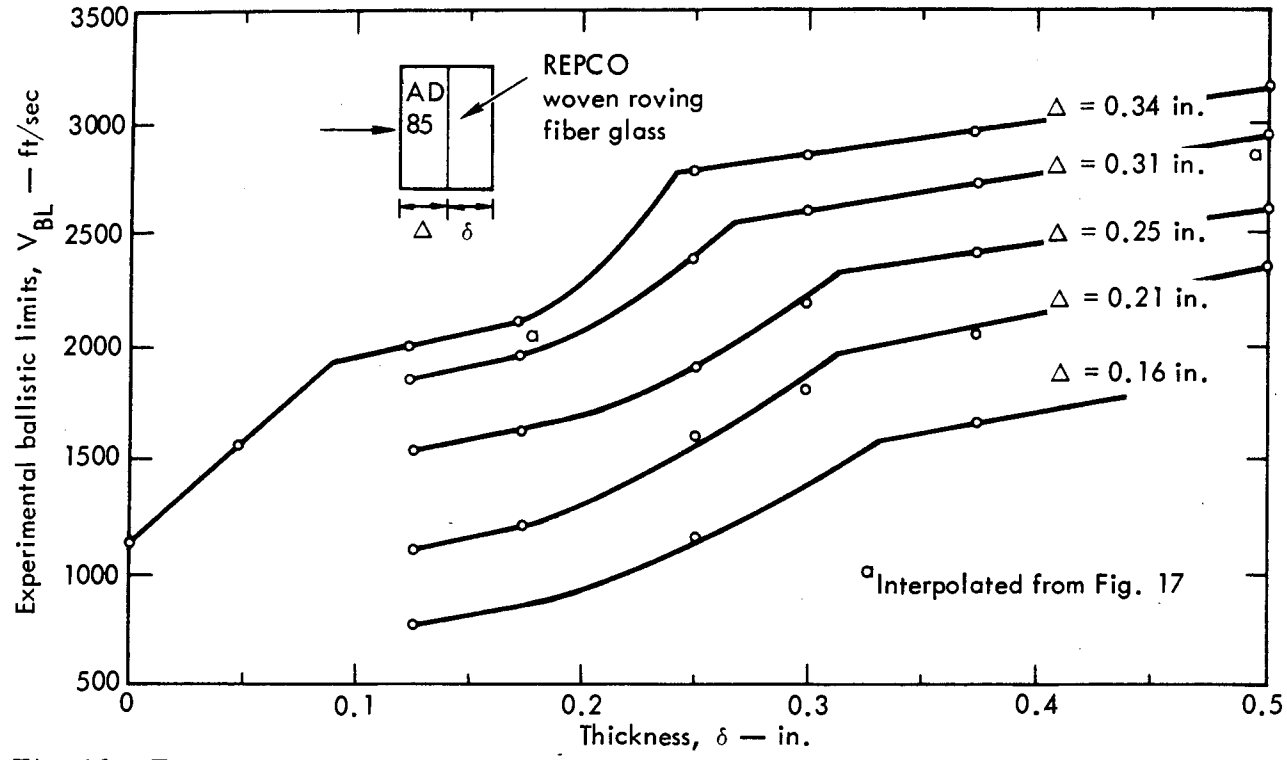

Fig. 16. Experimental ballistic limits for Coors AD85 alumina bonded to REPCO woven roving fiber glass (30-calibre sharp projectiles). Straight-line segments are shown linked without prejudice as to actual curve shape.

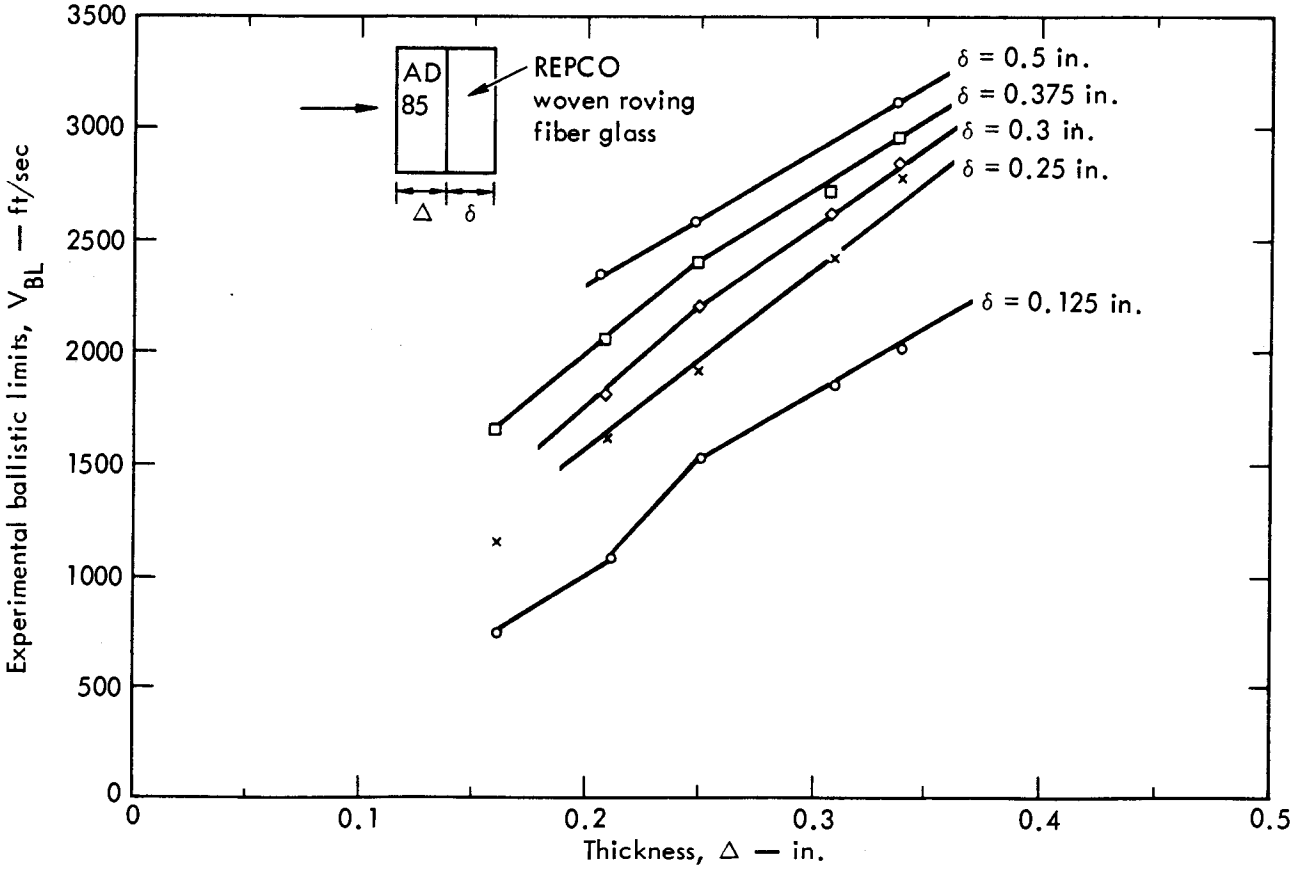

Fig. 17. Experimental ballistic limits for Coors AD85 alumina bonded to REPCO woven roving fiber glass (30-calibre sharp projectiles).

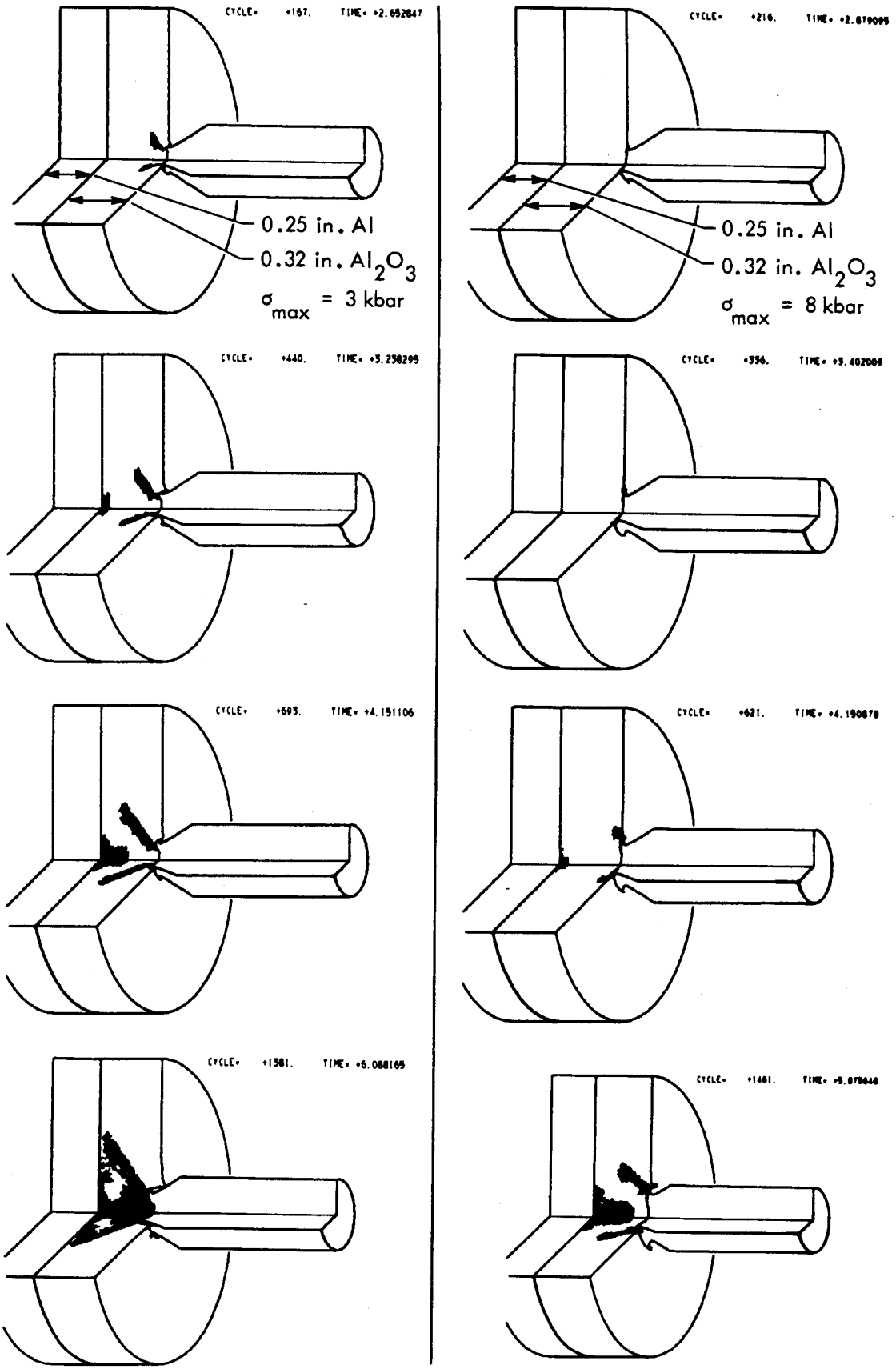

Fig. 18. Effect of fracture strength on time for fracture (left column: fracture strength = 3-kbar tension; right column: fracture strength = 8-kbar tension).

and the fibers. Since the desirable properties of the composites are revealed only in a dynamic environment, a simple dynamic testing procedure was developed to screen new composite materials (Appendix B).

Backup Plate Studies

The role of the backup plate is to support the ceramic fracture conoid at early times after the projectile impact and thus delay the breaking up of the ceramic. Eventually the conoid is completely broken, and the load on the backup plate is transmitted over smaller and smaller areas. The backup plate is now required to deflect in order to avoid high shear stresses due to the application of the load over an area smaller than the base of the conoid. The broken ceramic is effective in defeating the projectile when it is held in place because it is stiff to compression loads, and friction makes it difficult for the projectile to move material aside. Thus it would obviously always be better to have a rigid backup plate to hold the broken ceramic in place except that shear failure becomes the weakest link. Therefore the optimum backup plate design is a plate just stiff enough to avoid shear failure by the applied load. The energy of the impact is absorbed by the deflection of the backup plate, necessitating that the backup plate be able to undergo the excursion required to absorb the energy before a tensile failure occurs at the rear of the plate; i.e., the plate is required to have some minimum tensile elongation before failure.

The design of a backup plate would be straightforward except that in addition to the above properties it is required to have a low areal density. Actually this set of requirements has been the basis for developing materials for applications other than armor. In Table II the experimental ballistic limits are given for several materials selected for high strength-to-density ratios.

Some of the points discussed earlier are demonstrated in the results shown in Table II. The shear strength of aluminum 7079-T6, for example, is greater than that of aluminum 6061-T6, and there is a corresponding increase in the ballistic limits, V_{BL}. The strength of aluminum 2024-T4 is also superior to that of 6061-T6, but it was found that with dynamic loads the elongation property is inferior.

The TRIP steel used in Experiment 8 is a high-strength, high-elongation material. However, in order for steel to be competitive in weight with a low-density backup plate like aluminum, the steel plate must be thinner. Even though the strength and elongation properties of the TRIP steel are superior to those of aluminum, the thin steel plate is not stiff enough to support the ceramic as well as an aluminum plate of comparable weight (see Experiment 2). The loss of plate stiffness, which varies as the cube of the thickness, is responsible for the lower ballistic limit for the TRIP steel compared to that for the aluminum backup plates.

Table II. Experimental ballistic limits for 30-calibre sharp projectiles and targets of AD85 with different backup plates

Experiment	AD85 thickness (in.)	Backup plate	Target areal density (lb/ft^2)	Ballistic limits (ft/sec)
1	0.34	0.25-in. REPCO woven roving	8.62	2780 ± 50
2	0.34	0.25-in. 6061-T6 aluminum	9.52	2850 ± 50
3	0.34	0.25-in. 2024-T4 aluminum	9.52	2700 ± 50
4	0.34	0.25-in. 7079-T6 aluminum	9.52	2975 ± 50
5	0.34	0.125-in. Ti-120 VCA	8.93	2850 ± 80
6	0.34	0.25-in. Mg-Th	8.31	2100 ± 50
7	0.34	0.25-in. Lockalloy	8.72	2275 ± 50
8	0.34	0.09-in. TRIP[a] steel	9.71	2500 ± 50
9	0.34	0.062-in. Ti-120 VCA ± 0.125-in. REPCO woven roving	8.77	2275 ± 50
10	0.34	0.25-in. Be vacuum brazed to 0.062-in. Ti-120 VCA	9.85	3000 ± 100
11	0.31	0.25-in. Be vacuum brazed to 0.062-in. Ti-120 VCA	9.32	2775 ± 50

[a]See Ref. 4.

The purpose of the titanium used in Experiment 9 was to protect the ceramic side of the fiber glass from the late time, high shear loads. This combination does not offer an improvement because the projectile defeat mechanism for fiber glass requires a large excursion. The titanium has very good dynamic elongation properties, but not enough to follow the excursion of the fiber glass. The titanium failed in tension, and the overall performance of this target is poorer than for an all-fiber glass plate of similar weight (see Experiment 1).

Beryllium is a light material that has the property of high-resistance-to-shear distortion for compressive loads, but a poor tensile elongation property. In Experiments 10 and 11 a titanium plate was vacuum-brazed onto the rear surface of a beryllium backup plate in order to support the fracture conoid in the beryllium that is known to occur from a ballistic impact. The resulting backup plate when compared to an aluminum 6061-T6 plate of comparable weight has:

1. A greater resistance to deflection
2. A higher resistance to the impact compression and subsequent shear distortion.
3. Less deflective ability before a tensile failure

The ballistic limits for these backup plates (Experiments 10 and 11) are about the same as those for an all-aluminum plate. The point here was to demonstrate that a backup plate with a high resistance to deflection is effective when the material also has a high resistance to compression deformation from the applied load. It would be expected that the ballistic limits would be higher if the beryllium had better elongation properties.

Role of Bond Between Ceramic and Backup Plate

The targets for the ballistic limit experiments reported here use a polyurethane bond (Scotchcast 221) to hold the ceramic and backup plates together. It was noted that the ballistic limit for targets of 0.34-in. AD85 backed by 0.25-in aluminum dropped by ~250 ft/sec when a bond was not used. A bond did not make a noticeable difference for ceramic thicknesses less than 0.25 in. The 250-ft/sec drop in ballistic limit is about a 10% effect and is considered to be significant. It was decided to determine the reason for this effect because a clue to improving armor materials might be revealed.

Experiments showed that the increase in ballistic limits for bonded target materials was independent of the bonding material used. It was also established that the bonding material was not required to adhere to either the ceramic or the backup plate. These results were obtained by allowing the adhesive material to cure with a 1/2-mil thick plastic sheet between the adhesive and the target materials. Thus there was no structural strength between the ceramic and the backup plate. It was also found that a lubricant (MoS_2—Molykote) could be used between a ceramic and an aluminum backup plate to obtain the same ballistic limit as that obtained when an adhesive bond was used. The conclusions are that the bond has no structural effect on the target, but instead has an effect on the ceramic surface. The irregular surface of the ceramics causes local tension stresses when a load is transmitted across the surface. The bonding material fills in the void of the irregular surface and serves as a coupling medium between the ceramic and the backup plate.

This hypothesis was checked by eliminating surface imperfections by carefully grinding a smooth surface on the ceramic. The resulting ballistic limits for bonded and unbonded ground ceramics were the same and equal to the value for the untreated ceramic bonded to a backup plate.

It should be pointed out that the compressibility of the plastic bonding materials will allow tensions to occur in the ceramic depending on the thickness of the bonding layer. These tensions are due to the ceramic expanding into the compressible material; i.e., the ceramic is not being supported. Therefore, if the bonding layer is too thick more harm than good will result in the ballistic limit.

Tension Strengthening of Ceramic

From the experiments described in the preceding section it is seen that AD85 alumina is very sensitive to the treatment of the surfaces. These results are interpreted as showing the weakness of a ceramic to a tensile stress. It was thought that an improvement in the ballistic limit might result if the ceramic surface at the

backup plate could be prestressed in compression. The ceramic would then be capable of undergoing more distortion before a tensile failure state occurred. Specimens of AD85 alumina were quenched from 1450°C in a silicone solution. The differential cooling of the surfaces of the ceramic compared to the interior prestresses of the surfaces due to the differences in thermal expansion of the alumina and the glass phase. Three-point flexural tests showed a 100% improvement in the rupture modulus for the prestressed samples. For the target described in the preceding section there was the same 10% increase in ballistic limit for the quenched ceramic as there was for ceramics with ground surfaces (the effects are not additive).

The point here has been to establish the sensitivity of the ballistic performance to improvements in the tensile properties of a ceramic. In Fig. 6 it is seen that the rate of energy loss of the projectile is very high at ~7 μsec after impact. If this high rate of energy loss were sustained even a microsecond longer, a large improvement in ballistic performance would be expected. Therefore the time scale for the fracture and breakup of the ceramic is very important.

A calculation was made to determine how much delay in the development of the ceramic fractures might be expected if the tensile strength of the ceramic were increased. The calculation shown in Fig. 1 was repeated with the fracture strength changed from 3-kbar tension to 8-kbar tension. Figure 18 shows the two problems at the same time after impact. It is seen that there is a time difference of the order of a microsecond between the two problems when the development of the fracture pattern is about the same. Therefore, a ceramic with improved tensile strength would be expected to have a superior ballistic limit.

References

1. M. L. Wilkins, C. A. Honodel, and D. R. Sawle, An Approach to the Study of Light Armor, Lawrence Radiation Laboratory, Livermore, Rept. UCRL-50284 (June 1967).
2. M. L. Wilkins, Second Progress Report of Light Armor Program, Lawrence Radiation Laboratory, Livermore, Rept. UCRL-50349 (November 1967).
3. John Taylor, Los Alamos Scientific Laboratory, New Mexico, private communication (1968).
4. American Society for Metals Transactions Quarterly 60, 252 (June 1967).
5. A. L. Florence and T. J. Ahrens, Interaction of Projectiles and Composite Armor, U. S. Army Materials Research Agency, Watertown, Massachusetts, Rept. AMRA CR 67-05 (F) (January 1967).

Appendix A.

Derivation of Equation of State from Hugoniot Elastic Limit Experiments

In contrast to fluids, solids resist shear distortion. Following elasticity theory, the stress due to distortion is considered to be a linear function of the strain. There is an upper limit to the magnitude of the distortion stress, and this limit is stated by a yield condition. After the yield point has been attained for an elastic-plastic material, the material deforms plastically. A material is said to be elastic when the stress is proportional to strain, and plastic when the stress is no longer proportional to strain. Elastic-plastic theory has been found to apply very well to describe the behavior of ceramics. For compression loads the materials behave like elastic solids up to the yield point. After the yield point has been reached the material has been permanently changed or transformed so that it no longer follows the original stress-strain behavior. Thus for a ceramic it will be assumed that Von Mises yield condition states the condition when the material transforms from an elastic solid to a material with a different stress-strain behavior. The point here is that it is not necessary to consider the material plastic to apply the theory.

Some of the outstanding features of a material that has a yield stress can be demonstrated by considering a compression wave due to one-dimensional strain. For one-dimensional strain in the X-direction, the stress, σ_x, is given by:

$$\sigma_x = P + s_x$$

where pressure

$$P = K\left(\frac{V^o - V}{V}\right)$$

Distortion stress,

$$s_x = \frac{4}{3}\mu\left(\frac{V^o - V}{V}\right)$$

K = bulk modulus

μ = shear modulus

V = specific volume

In the above, P and s_x are both considered to be positive in compression.

In the model used here to describe the behavior of a ceramic, these equations apply until s_x reaches a maximum value, $s_x = 2/3\ Y$, where Y is the yield strength. For subsequent compression loading s_x remains constant and equal to the maximum value while P increases. The parameter K is initially constant but then increases with increasing pressure. Shocks can form with this description, and the Hugoniot equations apply when the pressure, P, is replaced by the total stress, σ_x.

In Fig. A1, point A is where the distortion stress component, s_x, has reached its maximum value and is referred to as the Hugoniot elastic limit. The discontinuous decrease in slope at point A will

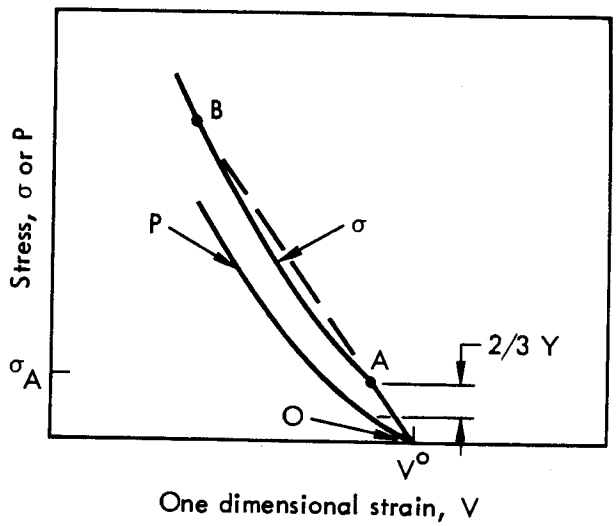

Fig. A1. Stress as function of one-dimensional strain.

cause the stress wave to break into two steps for stress levels that are between points A and B. An elastic precursor of stress level, σ_A, will travel at the elastic precursor velocity, C_E:

$$C_E^2 = \left[\frac{K + (4/3)\mu}{\rho^o}\right]$$

This stress will be followed by a shock traveling through the now transformed material with the shock velocity, S_T. From the Hugoniot equations:

$$S_T^2 = V_A^2\left(\frac{\sigma - \sigma_A}{V_A - V}\right)$$

where

$$V = \frac{1}{\rho}$$

$$\sigma_A < \sigma < \sigma_B$$

For $\sigma > \sigma_B$ the shock wave velocity in the transformed material will be greater than the elastic precursor velocity, C_E, and the stress will propagate as a single shock. This follows from noting that the slope of the line connecting point O with a stress point above σ_B will be greater than the slope OA.

The experimental Hugoniot elastic limits and higher stress points were measured for several ceramic materials. The stress waves were obtained from charges of high explosives ignited by a plane wave lens. An aluminum plate was used between the explosive and the ceramic sample to obtain the input stress level by a measurement of the free surface velocity of the aluminum and to obtain a flat-topped wave profile. The details of this experimental technique have been well described by Florence and Ahrens.[5] Ultrasonic velocity measurements taken at a frequency of 10 mH_Z allow the elastic constants to be calculated:

Shear wave velocity,

$$C_s^2 = \frac{\mu}{\rho^o}$$

Longitudinal wave velocity,

$$C_E^2 = \frac{K + (4/3)\mu}{\rho^o}$$

With this information, an equation of state can be made using the form described in the first progress report.[1] (The departure from the Von Mises condition for tension states has been discussed separately.)

Figures A2 and A3 show a calculation of the one-dimensional strain experiment used to obtain the equation-of-state parameters for boron carbide. The magnitude of the calculated free surface velocity agrees with the experiment because it was part of the input to the calculation. The magnitude of the calculated free surface

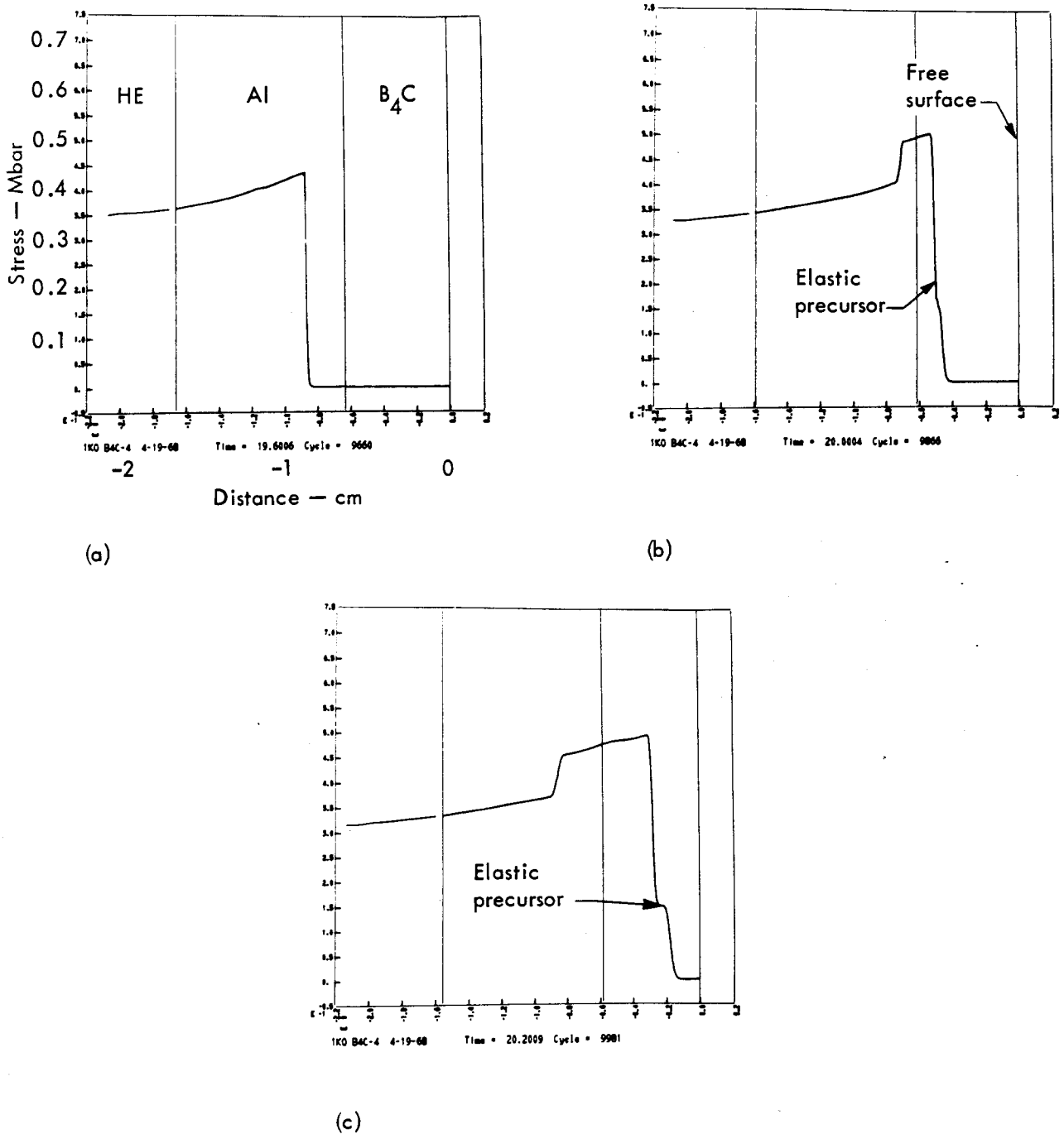

Fig. A2. Calculated stress-spaced profile of high-explosive-induced stress wave in aluminum and boron carbide.

velocity due to the arrival of the shock wave through the transformed material also agrees with the experiment. This latter result is due to the theory.

Experimental data in a form suitable for use in an equation of state are given for several ceramics in Table AI and Figs. A4 through A8.

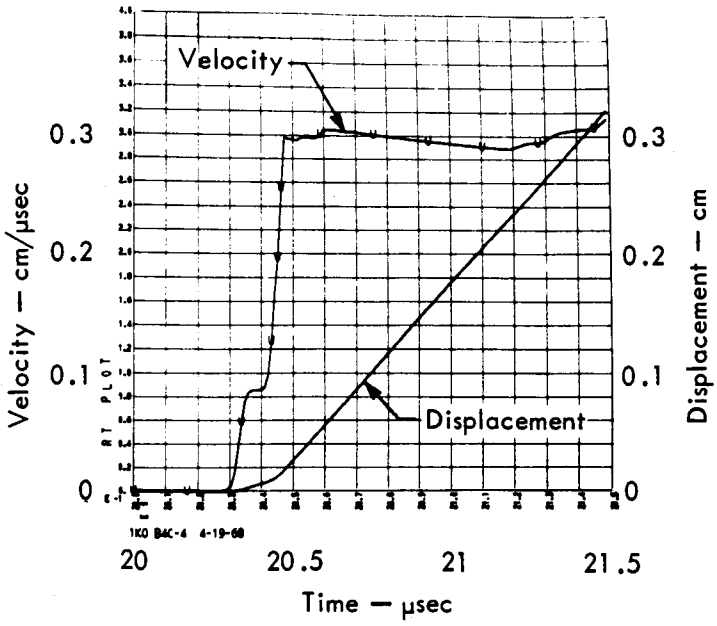

Fig. A3. Calculated boron carbide free surface velocity and free surface displacement as function of time.

Table AI. Elastic constants.[a]

Material	Density (g/cm^3)	Bulk modulus K (Mbar)	Shear modulus μ (Mbar)	Sound speed C (cm/μsec)	Hugoniot elastic limit	Yield strength Y° (Mbar)	Elastic impedance $\rho°$ C
Coors AD85 alumina	3.43	1.54	0.83	0.88	0.06	0.038	3.02
Diamonite alumina	3.72	1.93	1.27	0.99	0.08	0.057	3.68
WESGO 995 alumina	3.81	2.14	1.41	1.03	0.084	0.060	3.92
Hot-pressed alumina	3.92	2.50	1.49	1.07	0.140	0.093	4.19
Boron carbide	2.50	2.63	1.65	1.39	0.150	0.102	3.48
Beryllium oxide	2.84	1.85	1.43	1.15	0.085	0.064	3.27

[a]A similar table appeared in the second progress report. Because of additional data since publication of that report, values shown here differ from those appearing in the original table.

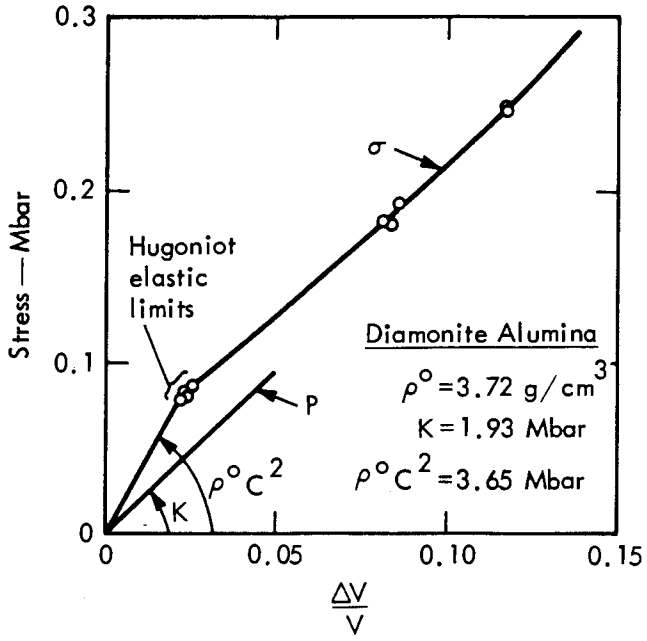

Fig. A4. Experimental data for diamonite alumina.

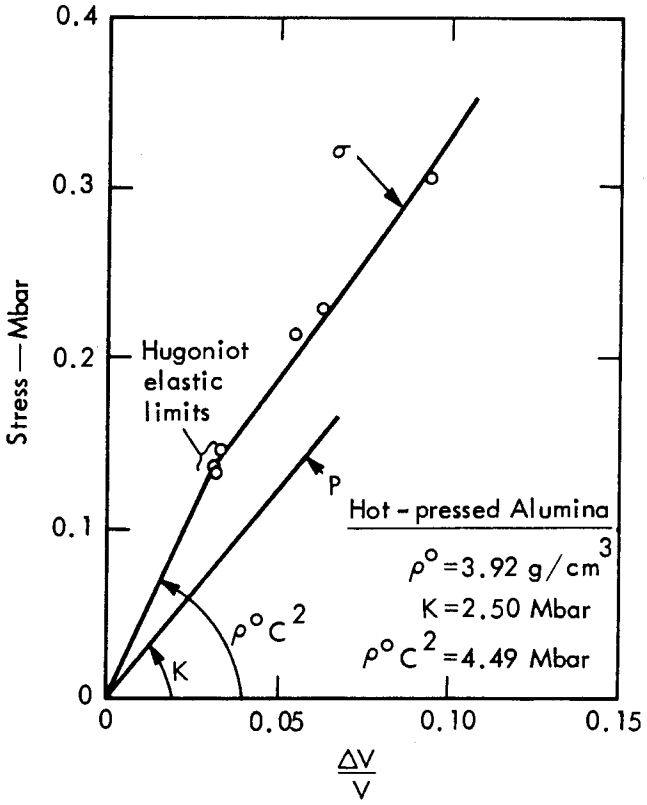

Fig. A5. Experimental data for hot-pressed alumina.

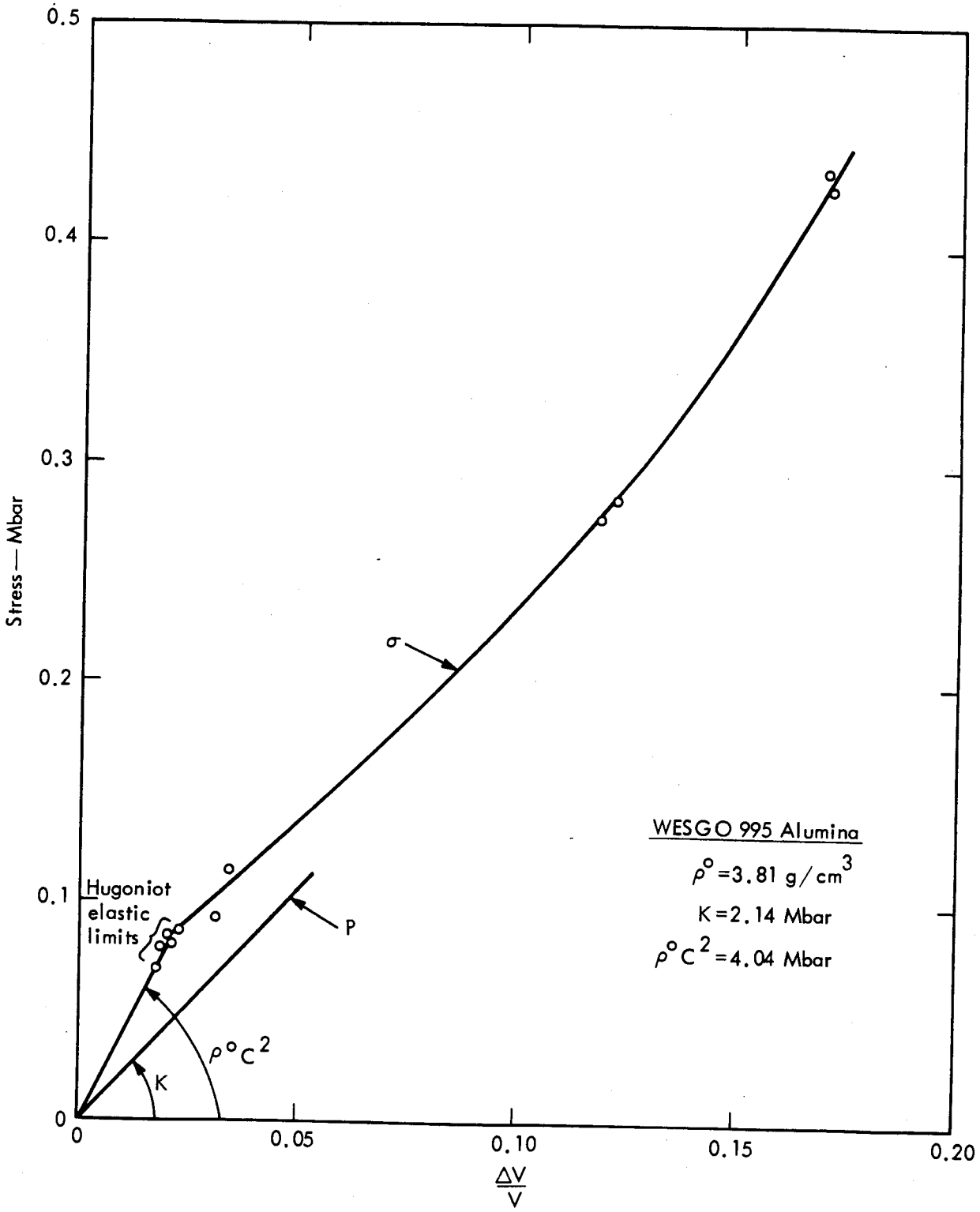

Fig. A6. Experimental data for WESGO 995 alumina.

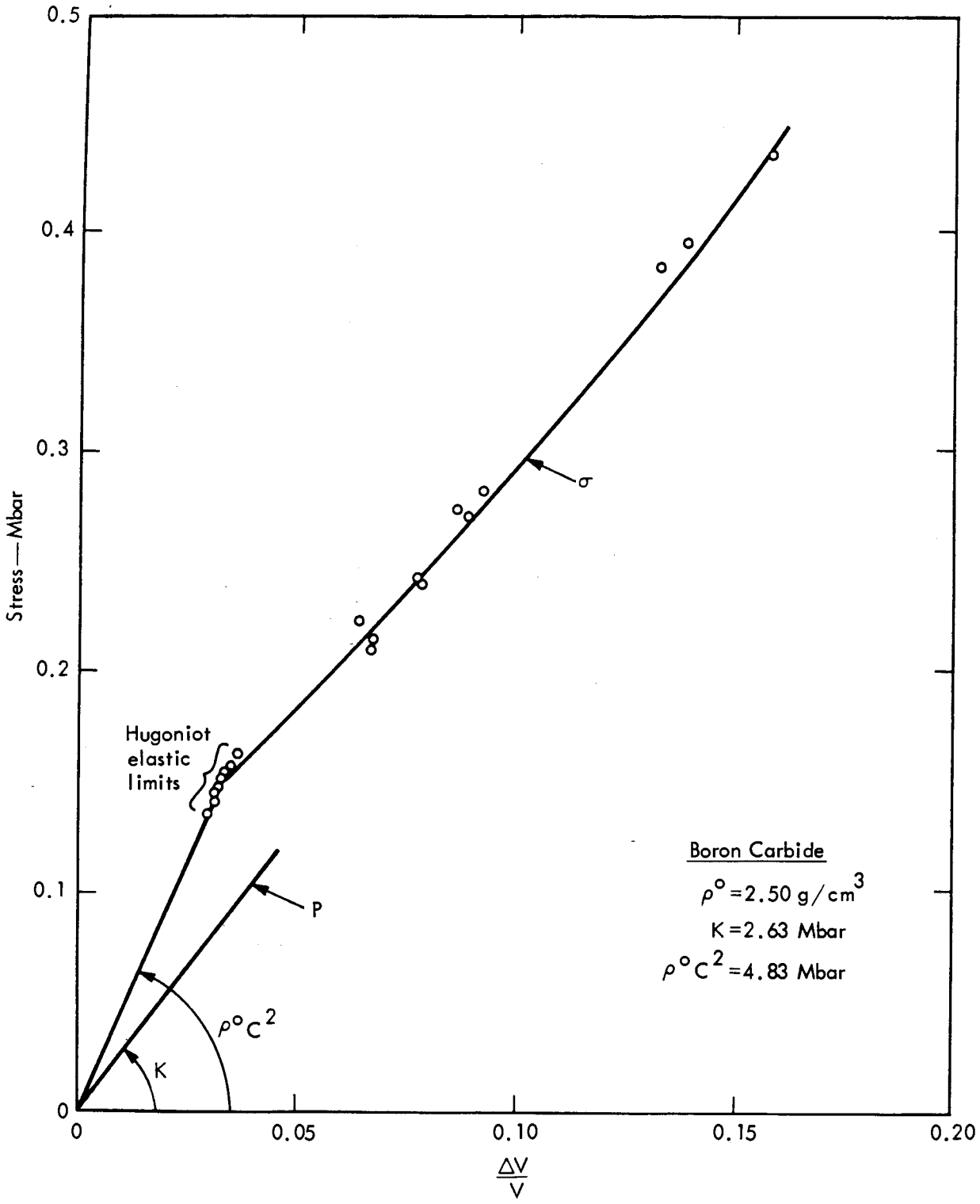

Fig. A7. Experimental data for boron carbide.

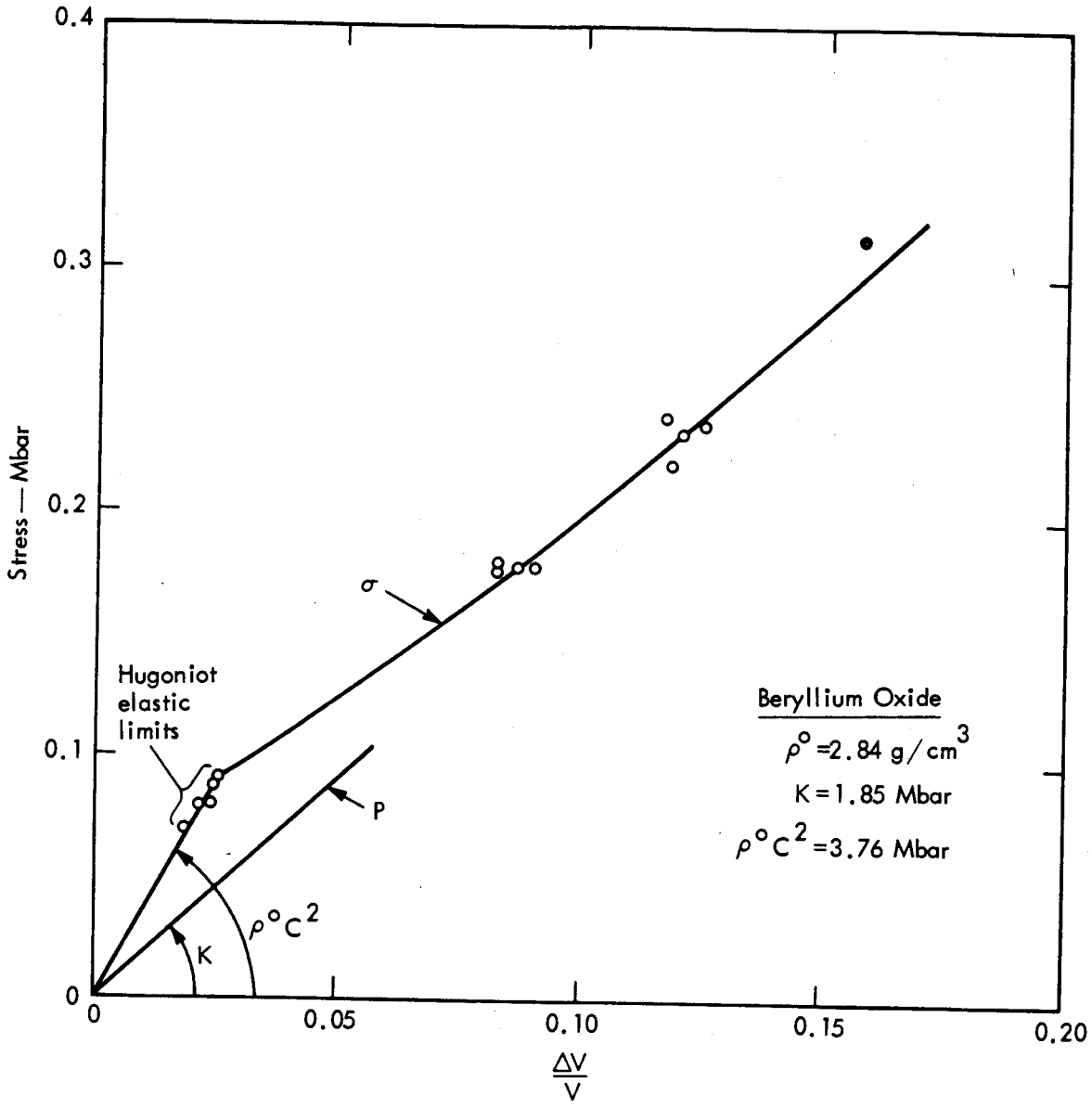

Fig. A8. Experimental data for beryllium oxide.

Appendix B.

Dynamic Testing Procedure for Screening New Composite Materials

Mechanical Testing of Backup Plates

There is a need for a simple mechanical test to evaluate materials for use as backup plates in ceramic-faced armor. The ordinary tension test yields important information, but it is very time consuming to prepare samples; it is easier to do the ballistic limit experiment. The Dynapak testing machine offers the possibility to evaluate materials under load conditions similar to the loading from a ballistic impact. In this test a ram is forced directly into the backup plate specimen. The displacement of the ram and the load on the ram by the plate are continuously measured. It is recalled that the ballistic load on the backup plate is first applied over an area corresponding to the diameter of the ceramic fracture conoid. Subsequently, the load is applied by the broken ceramic between the projectile and the backup plate over an area corresponding to the diameter of the projectile, 0.3 in. It was found that a ram with a 0.6-in. spherical diameter on one end reproduced about the same overall deformation to a ceramic-faced backup plate as a ballistic test with a 30-calibre projectile. To evaluate the resistance of the backup plate to shear loads, a blunt 0.3-in. diam ram is used.

As discussed earlier, the backup plate is required to have a balance between stiffness and flexibility. A higher resistance to shear is necessary for stiffer backup plates. Aluminum 6061-T6 and woven roving (REPCO) fiber glass were chosen as standards that characterize stiffness and flexibility, respectively. The Dynapak load-vs-displacement measurements for these materials are shown in Figs. B1 and B2.

The tests correlate very well with ballistic data. The stiffness of the plate is related to the slope of the load curves, Figs. B1 and B2. It is seen that aluminum 7079-T6 has better characteristics than aluminum 6061-T6. The corresponding ballistic limits for 0.34-in. AD85 facings are:

1. 0.25-in. Al (7079-T6)—
   $V_{BL} = 2975 \pm 50$ ft/sec
2. 0.25-in. Al (6061-T6)—
   $V_{BL} = 2850 \pm 50$ ft/sec

The relatively low stiffness, but very large deflection capability of woven roving is seen in Fig. B1. The G-10 fiber glass shown in this figure has very good tensile properties, but the ballistic limit was very low compared to woven roving. It is seen that the Dynapak data correlate in the same manner.

The effect of using laminates instead of a single backup plate and the effect of using a smaller ring mount, discussed earlier in regard to ballistic performance, can also be demonstrated with this test.

Figure B3 shows that the slope of the aluminum loading curve is reduced, and thus the plate stiffness, when two plates replace a single plate of the same total

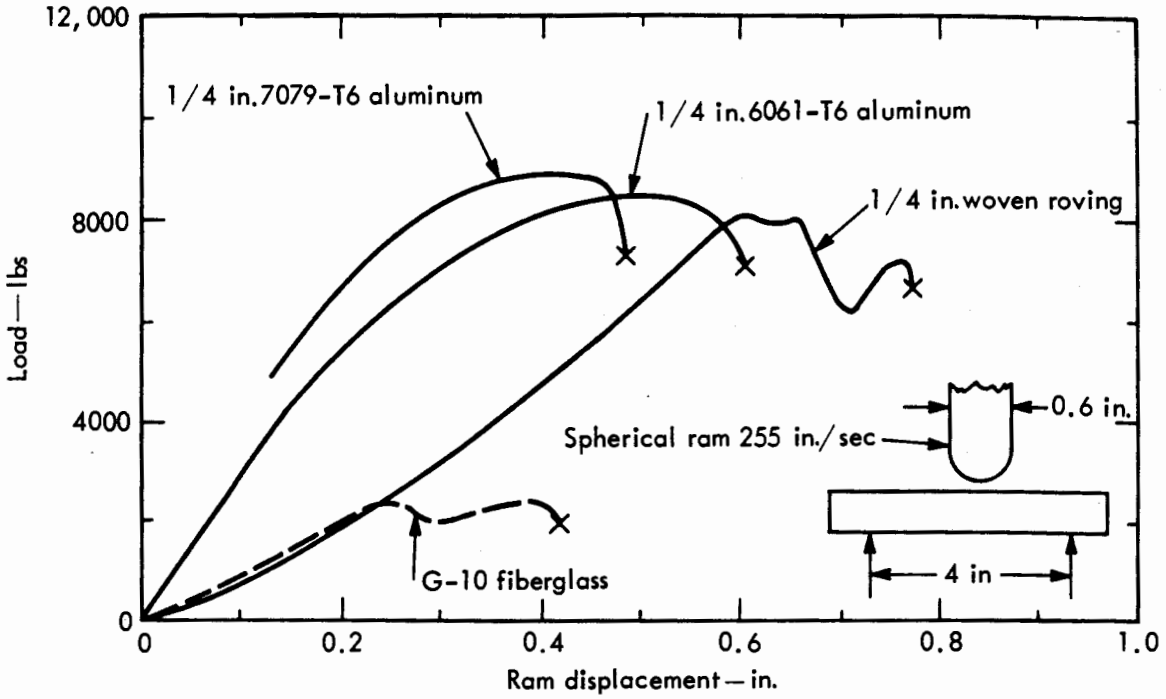

Fig. B1. Plate deflection test.

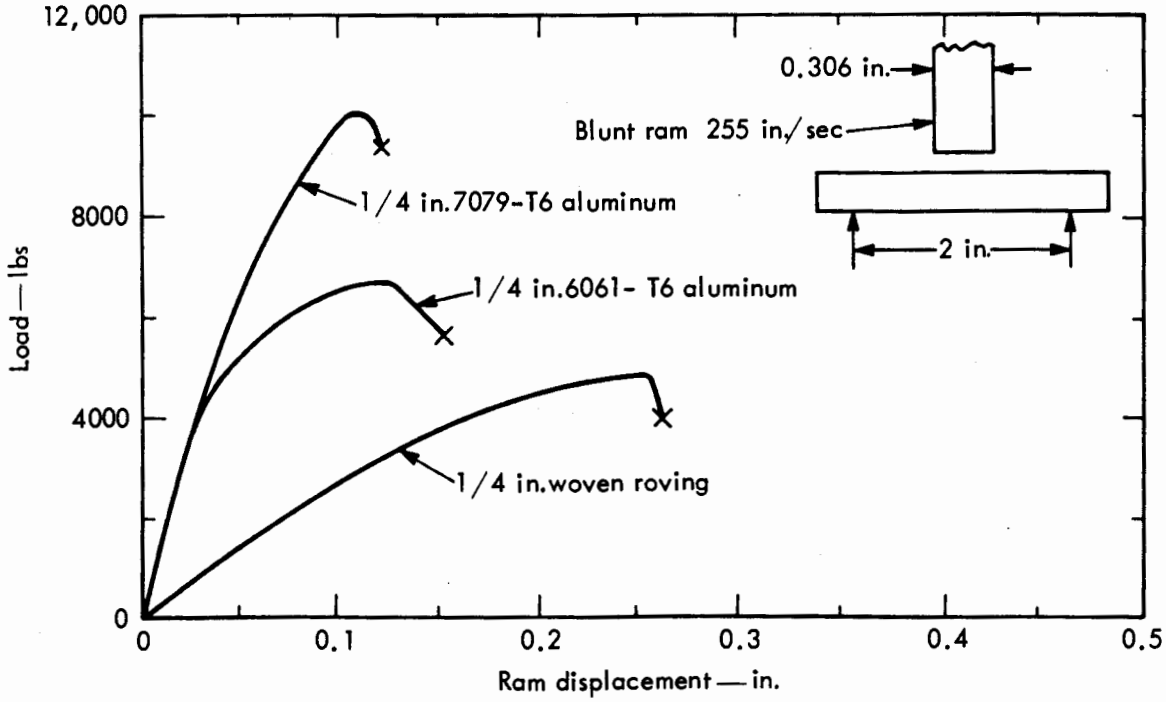

Fig. B2. Plate resistance to shear test.

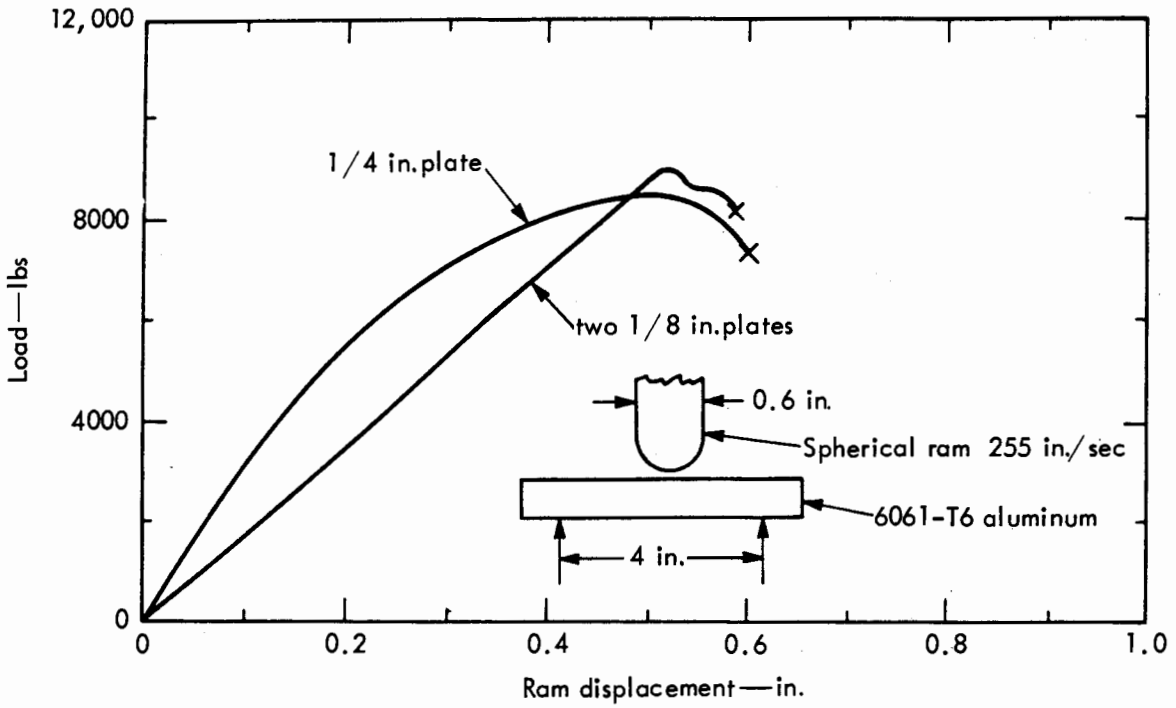

Fig. B3. Deflection of single and laminated plates.

thickness. It is seen that the total deflection to failure is the same. When two plates were used the ballistic limit dropped because of the loss in rigidity. Similar experiments were conducted with woven roving. The total deflection at failure was the same for one 0.25-in. plate or two 0.125-in. plates. However, the maximum load at failure was less for the two-plate experiment. The ballistic limit, as pointed out earlier, is about the same for these cases since the important characteristic of a fiber glass backup plate is the large deflection capability.

The effect on the target ballistic limit for small ring mounts is demonstrated in Fig. B4. The smaller ring severely limits the important excursion characteristic of the fiber glass and the ballistic limit decreases.

Target: 0.34-in. AD85 backed by 0.25-in. woven roving

1. 4-in. ring mount— V_{BL} = 2780 ± 50 ft/sec
2. 2-in. ring mount— V_{BL} = 2350 ± 50 ft/sec

For aluminum, the smaller ring mount increases the stiffness of the plate, but decreases the excursion. The ballistic limit remains about the same.

Target: 0.34-in. AD85 backed by 0.25-in. 6061-T6 aluminum

1. 4-in. ring mount— V_{BL} = 2850 ± 50 ft/sec
2. 2-in. ring mount— V_{BL} = 2900 ± 50 ft/sec

The results shown in Fig. 1 for 6061-T6 aluminum were the same, within experimental error, when the ram velocity was reduced from 255 to 80 in./sec. Thus no dynamic effects were detected. The actual ballistic load, however, is applied at a rate of ~10 times greater than the 255 in./sec used here. (The projectile

impact velocity on the target is of the order of 100 times the Dynapak ram velocity; however the actual ballistic load rate on the backup plate is only a tenth of the projectile velocity.)

A large rate effect was found from the Dynapak tests with woven roving (REPCO). In Fig. B5 it is seen that the desirable backup plate characteristics are present only at high rates of loading. This is a very significant result because it points out that for some materials the static properties cannot be correlated with the ballistic behavior. For example, the static properties of the G-10 fiber glass mentioned earlier are superior to those of the woven roving fiber glass. The ballistic results with G-10 fiber glass were very poor (V_{BL} = 1925 ± 50 ft/sec compared to V_{BL} = 2780 ± 50 ft/sec for woven roving where the ceramic face is 0.34-in. AD85). The reason is made clear with the Dynapak tests. Figure B1 shows that G-10 fiber glass is inferior to the woven roving at the load rate of 255 in./sec in both maximum total load and total deflection before failure.

Calculation of Rupture Failure of Aluminum Plate

A calculation of the Dynapak experiment shown in Fig. B1 for 6061-T6 aluminum was made using the rupture criteria described in Appendix C. For economy of calculational time, the calculation used a faster ram velocity (0.01 cm/μsec) than that used in the experiment. The calculation, Fig. B6, shows that a radial crack occurs at the rear surface of the aluminum plate when the ram displacement is

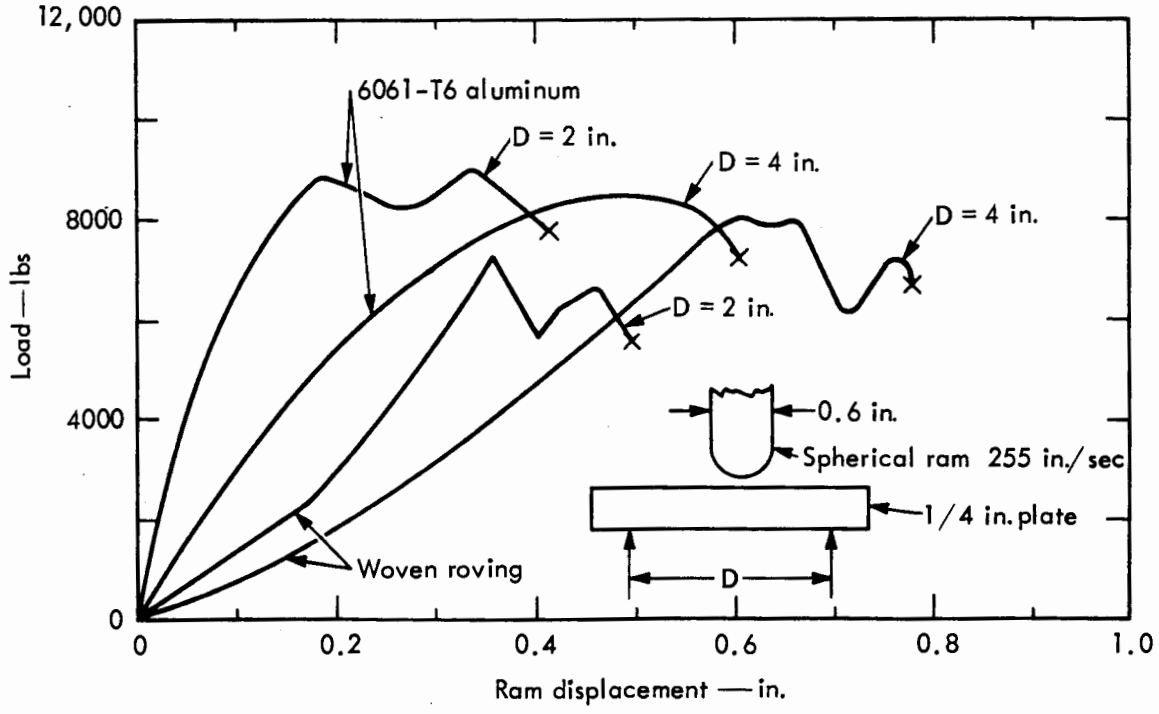

Fig. B4. Effect of ring mount diameter, D, on plate deflection.

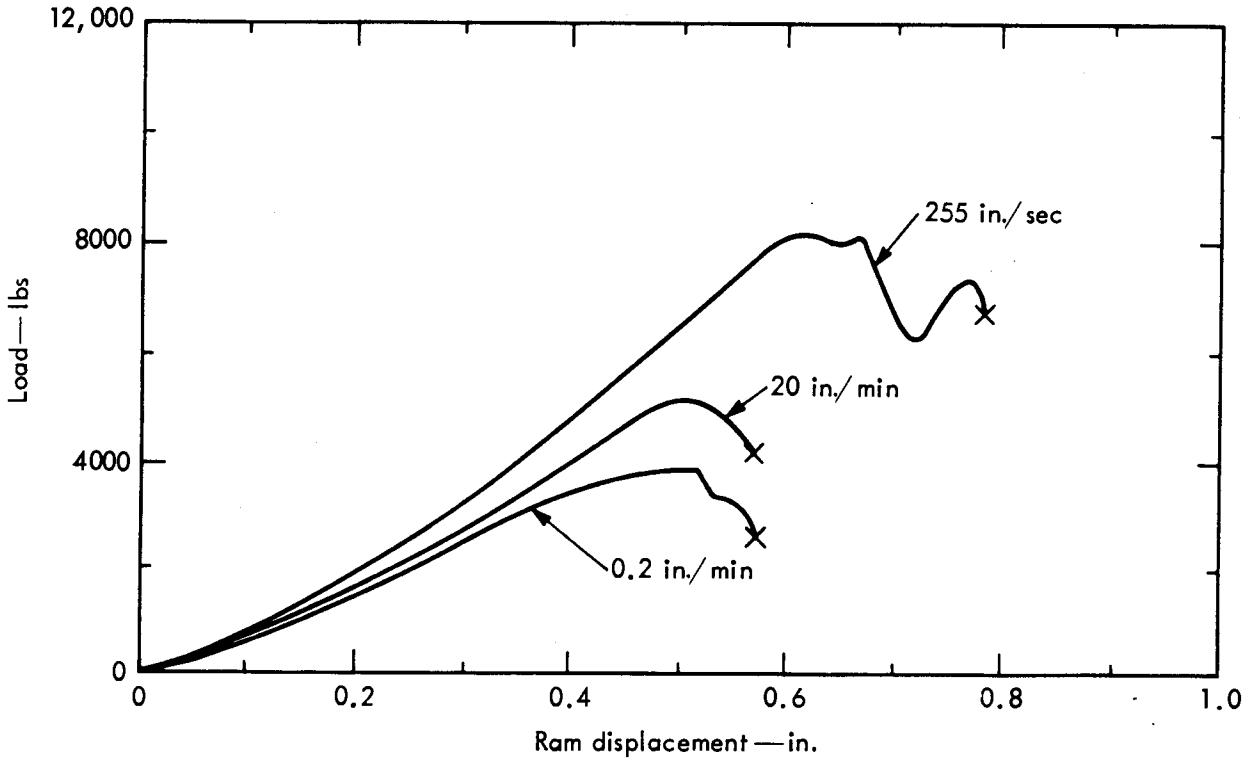

Fig. B5. Effect of ram velocity on load deflection of 1/4-in. woven roving (0.6-in. diam spherical ram; 4-in. diam ring mount).

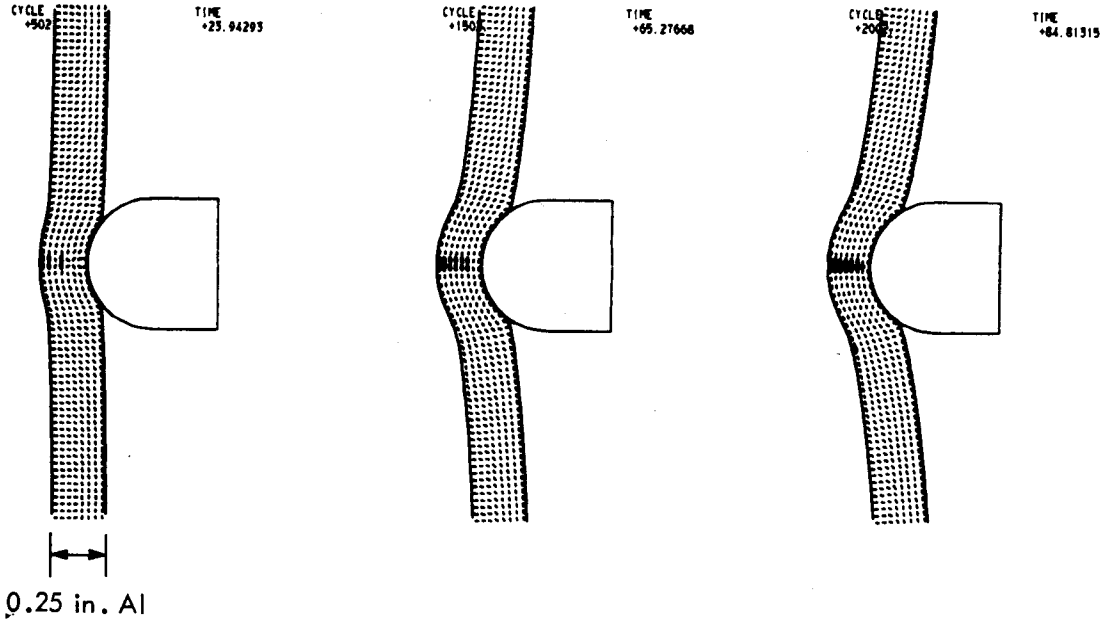

Fig. B6. Calculation of Dynapak test on aluminum (lines show directions of maximum principal stresses; circles show positions where σ_θ stress has reached 3.5-kbar tension; line on axis is when $\sigma_{max} > 3.5$ kbar and $\gamma > 0.21$).

0.26 in. The crack reaches the ram after a ram displacement of 0.33 in. The failure is from the hoop stress, σ_θ, and, since, it occurs first at the axis, the crack can be calculated with the two-dimensional program. In the experiment the subsequent failure after the axial crack is by radial cracks that emanate from the axial crack. The calculation can thus predict the beginning of the plate failure. It would require a three-dimensional calculational program to carry this type of failure to completion, but nothing new for this problem would be expected from such a calculation.

Appendix C.

Tension Test

There are two kinds of material strength: (1) a resistance to plastic flow, and (2) a resistance to rupture. The Von Mises yield criterion treats resistance to plastic flow and describes the limit of the elastic resistance where subsequent loading leads to plastic flow. For the materials of interest as backup plates for ceramic composite armor, the elastic limit occurs at strains less than 1%. The rupture of the materials occurs at strains of the order of 10%. The strength of a material in armor is utilized up to the ultimate failure by rupture. Thus for the greatest part of the loading the material has already failed elastically and is in the plastic flow regime. It is important to understand the strength of a material in the plastic flow regime and the conditions for the ultimate failure by rupture.

The simple tension test affords an experiment that examines the elastic limit of a material and the subsequent failure by rupture. The experiment measures the elongation of a unit length of the test specimen as a function of the applied tension load. It is of interest to perform a calculation of this experiment with the two-dimensional elastic-plastic code. The objects are the following:

1. To compare the interior state of the material as determined by exterior measurements on the test sample with the interior state of the material calculated by the code

2. To establish a rupture criterion

The calculation considered an aluminum rod pulled at both ends by a constant velocity (Fig. C1). The calculation reproduced the familiar contraction at the rod

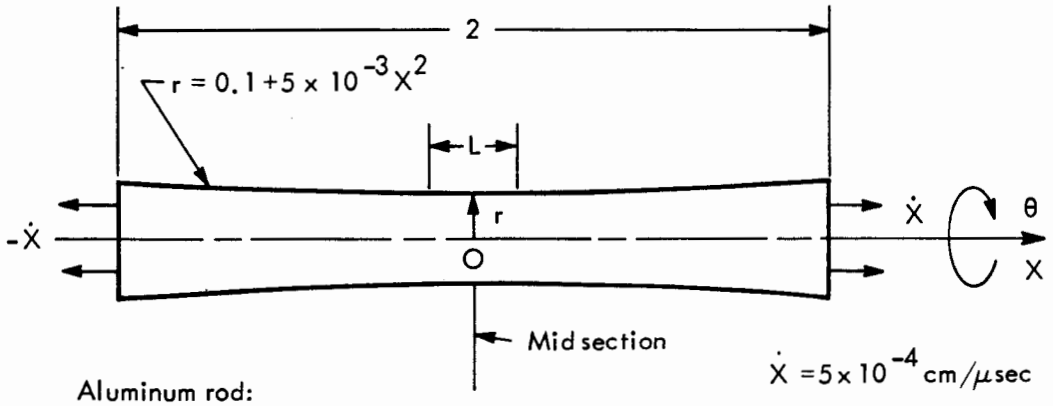

Aluminum rod:

Pressure: $P = -0.73 \ln V/V_o$ (Mbar)

Density: $\rho^o = 2.7$ g/cm^3

Shear modulus: $\mu = 0.248$ (Mbar)

Yield strength: $Y^o = 0.003$ (Mbar)

Fig. C1. Original geometry of rod pulled in both directions along X-axis.

center. It also showed that for large strains the principal stresses corresponded to the coordinate axes and that the stresses and strain were constant through a given cross section. This means that an analysis with measurements made on the outside surface of the rod, as can be done experimentally, can in fact describe the conditions of stress-strain in the rod interior.

If a length, L, is measured along the surface of the rod and a radius, r, is measured at the rod midsection then the natural strains can be expressed as:

$$\epsilon_x = \int_{L^o}^{L} \frac{dL}{L}$$

$$\epsilon_r = \int_{r^o}^{r} \frac{dr}{r} \qquad \text{(C1)}$$

$$\epsilon_\theta = \int \frac{dr\, d\theta}{r\, d\theta} = \int \frac{dr}{r}$$

where L^o and r^o are the initial lengths. It should be noted that these are not the definitions of strain used in the Hemp code.

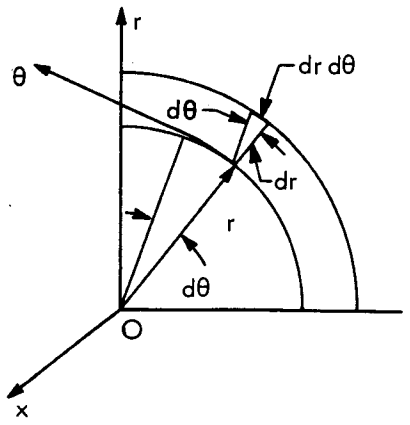

The strain ϵ_θ is the result of the change in length of a lineal element in the θ-direction where the change in length is due to a displacement in the r-direction.

The concept of natural strain refers to the extension of an element to the current length rather than to the initial length.

The volumetric strain $\int \frac{dV}{V}$ is:

$$\int \frac{dV}{V} = \int [\epsilon_x + \epsilon_r + \epsilon_\theta] = \int [\epsilon_x + 2\,\epsilon_r]$$

From Eq. (C1):

$$\ln \frac{V}{V^o} = \ln \frac{L}{L^o} + 2 \ln \frac{r}{r^o}$$

Hence,

$$\frac{V}{V^o} = \left(\frac{L}{L^o}\right)\left(\frac{r}{r^o}\right)^2 \qquad \text{(C2)}$$

where

V^o = initial volume.

In the tension test experiment the load is a measured quantity. In the calculation the stress at one end of the rod, σ_{end}, can be considered to be the measured stress. The stress at the rod center, σ_x, can be calculated:

$$\sigma_x = \left(\frac{r_{end}}{r}\right)^2 \sigma_{end} \qquad \text{(C3)}$$

where r_{end} is the radius at the position on the axis where the stress, σ_{end}, is recorded.

The strains, volume, and stress calculated with Eqs. (C1), (C2), and (C3) are shown in Fig. C2. Table CI shows the values of interior parameters of the rod calculated by the code. It is seen that values of parameters in Fig. C2 are the same as those shown in Table CI.

In the tension test the stress normal to the rod surface is zero. For elastic strains, the stresses in the directions of the coordinate axes are:

$$\sigma_x = -P + s_x$$
$$0 = -P + s_r$$
$$0 = -P + s_\theta \qquad \text{(C4)}$$

where s_x, s_r and s_θ are the stress deviators, and P, the pressure, defined as

$$s_x = 2\mu \left(\epsilon_x - 1/3 \ln \frac{V}{V^o} \right), \text{ etc.}$$

$$P = -K \ln \frac{V}{V^o}$$

Now, $\sigma_r = \sigma_\theta = 0$ since $\epsilon_\theta = \epsilon_r$; hence $s_r = s_\theta$.

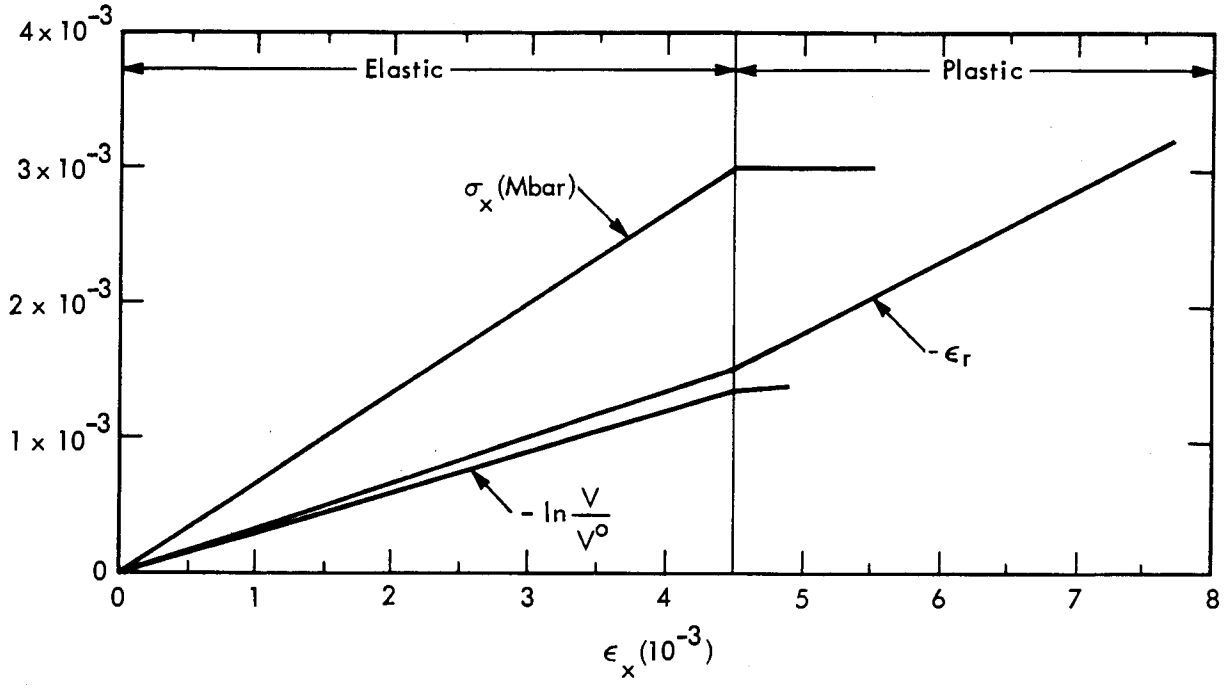

Fig. C2. Calculated rod parameters using exterior measurements [Eqs. (C1), (C2), and (C3) with $L^o = 0.1$ and $r^o = 0.1$].

Table CI. Parameters calculated on axis at midsection of rod (Fig. C2). (Total stress is $\sigma_x = -P + s_x$, etc.)

Time (μsec)	Total strain components (10^{-3})			Plastic strain components (10^{-3})			$\ln \frac{V}{V^o}$ (10^{-3})	Pressure (kbar)	Axial stress (kbar)	Stress deviators (kbar)		
T	ϵ_x	ϵ_r	ϵ_θ	ϵ_x^p	ϵ_r^p	ϵ_θ^p		P	σ_x	s_x	s_r	s_θ
A. Elastic												
4	2.045	-0.707	-0.709	0	0	0	0.629	-0.459	1.369	0.910	-0.455	-0.455
6	3.067	-1.058	-1.058	0	0	0	0.951	-0.694	2.058	1.364	-0.682	-0.682
8	4.135	-1.437	-1.437	0	0	0	1.26	-0.920	2.764	1.844	-0.921	-0.923
B. Plastic												
10	4.986	-1.802	-1.802	0.494	-0.247	-0.247	1.382	-1.008	3.008	2.000	-1.000	-1.000
12	7.336	-2.982	-2.967	2.84	-1.42	-1.42	1.387	-1.012	3.012	2.000	-1.000	-1.000
14	10.570	-4.594	-4.569	6.06	-3.04	-3.02	1.407	-1.026	3.026	2.000	-1.000	-1.000
41	151.23	-74.54	-74.68	146.53	-73.20	-73.33	2.010	-1.467	3.467	2.000	-1.000	-1.000

From the parameter shown in Fig. C1, where the elastic limit has not been exceeded, all of the elastic constants can be calculated:

Bulk modulus,

$$K = 1/3 \frac{(\sigma_x + \sigma_r + \sigma_\theta)}{\Delta} = 0.724$$

Poisson's Ratio,

$$\nu = \frac{\epsilon_r}{\epsilon_x} = 0.345 \qquad \text{(C5)}$$

Young's Modulus,

$$E = \frac{\sigma_x}{\epsilon_x} = 0.665$$

where

$$\Delta = \ln \frac{V}{V^o}$$

It is easily verified that the constants calculated above are almost identical to the input constants of the problem, μ and K (Fig. C2). It is recalled that:

$$\nu = \frac{3K - 2\mu}{6K + 2\mu} \quad \text{and} \quad E = \frac{9K\mu}{3K + \mu}$$

$$= 0.347 \qquad = 0.668$$

It is seen from Eq. (C4) that $s_r = P$. As the pull on the rod continues the stress combination at a point in the material reaches a limiting value imposed by the elastic yield condition. After this value has been attained plastic flow begins. From the boundary condition of the tension test and the Von Mises yield condition the stresses at the elastic limit are:

$$s_x = 2/3\ Y^o$$

$$s_r = s_\theta = -1/3\ Y^o \qquad \text{(C6)}$$

Hence

$$P = -1/3\ Y^o$$

where Y^o is the value of σ_x at the elastic yield point.

It should be noted that there is no limit imposed on the magnitude that P may attain. The yield condition influences only the magnitude of s_r. The flow in the elastic as well as the plastic region adjusts itself to maintain the boundary condition $\sigma_r = -P + s_r = 0$.

It is seen in Table CI that as the pull continues the magnitudes of the plastic strain components and hence the total strain components increase. The total strain can be considered the sum of the plastic and elastic strains:

$$\epsilon_x = \epsilon_x^p + \epsilon_r^e$$

$$\epsilon_r = \epsilon_r^p + \epsilon_r^e \qquad \text{(C7)}$$

$$\epsilon_\theta = \epsilon_\theta^p + \epsilon_\theta^e$$

where

ϵ = total strain

ϵ^p = plastic strain

ϵ^e = elastic strain

Plastic incompressibility is given by:

$$\epsilon_x^p + \epsilon_r^p + \epsilon_\theta^p = 0$$

It should be pointed out that the plastic incompressibility is not an imposed condition, but is a consequence of the mathematical formulation of the elastic-plastic

problem. The stress deviators are functions of the elastic components of the strain, Hooke's Law. It is implied in the formulation of the stress deviatiors that the total strain is equal to the sum of the elastic components of strain. Therefore, in Eq. (C7) it follows that the sum of the plastic components of strain is zero.

The above analysis considered an elastic perfectly plastic description for the aluminum rod. Experiments show that for aluminum 6061-T6 there is an increase in strength due to work hardening from 2.5 to 3.4 kbar. The above calculation considered a constant mean strength, Y^o = 3 kbar. The calculation was repeated where the material strength, Y^o, increased as a function of the intensity of plastic deformation, γ, so as to reproduce the experimental stress-strain results:

$$Y^o = 2.5 + \left(\frac{\gamma}{a + \gamma}\right)(0.9) \qquad \text{(C8)}$$

where

$a = 0.01$

$$\gamma = 2/3\sqrt{\left(\epsilon_1^p - \epsilon_2^p\right)^2 + \left(\epsilon_2^p - \epsilon_3^p\right)^2 + \left(\epsilon_3^p - \epsilon_1^p\right)^2}$$

ϵ_1^p, ϵ_2^p, ϵ_3^p = principal components of the plastic strain

When work hardening is included in the calculation, the strain is absorbed throughout the length of the rod and not localized at the rod midsection as it was for the constant yield stress calculation. To reach the same elongation at the rod center as the calculation without work hardening would require an increase in calculational time of perhaps a factor of ten. The calculation was therefore abandoned after an elongation of ~3%. The results did appear, however, to be following the same pattern as the constant yield strength calculation. A much more economical way of performing these two calculations would be to start with a narrow section already in the rod and use a smaller length-to-diameter ratio than the ratio of ten used here.

The calculations show that as the plastic flow progresses the plastic deformation in the center of the test specimen increases at a greater rate than the plastic deformation at the outside of the specimen. At the time the elongation measured at the outside of the specimen reached 12%, the experimental rupture elongation, the elongation in the interior of the specimen was ~15%. It is known from x-ray measurements made during tensile tests that the rupture starts from the interior of the specimen.

The radial distribution of stress and strain is constant at the rod midsection up to the elastic limit. At the elastic limit, the stress deviator in the direction of pull, s_x, is in tension. The radial stress deviator, s_r, and the hoop stress deviator, s_θ, are equal and in compression. As the pulling continues the necking of the midsection causes an increase in the compression of the hoop stress deviator, s_θ. There is a corresponding drop in the compression of the radial stress deviator, s_r, and a very slight decrease in the tension, s_x. The greatest change in the magnitudes of the stress deviators from the values at the elastic limit occurs in the radial stress deviator, s_r, at the rod exterior (Fig. C3).

The boundary conditions at the rod exterior, $-P + s_r = 0$, implies that the pressure P must decrease in magnitude

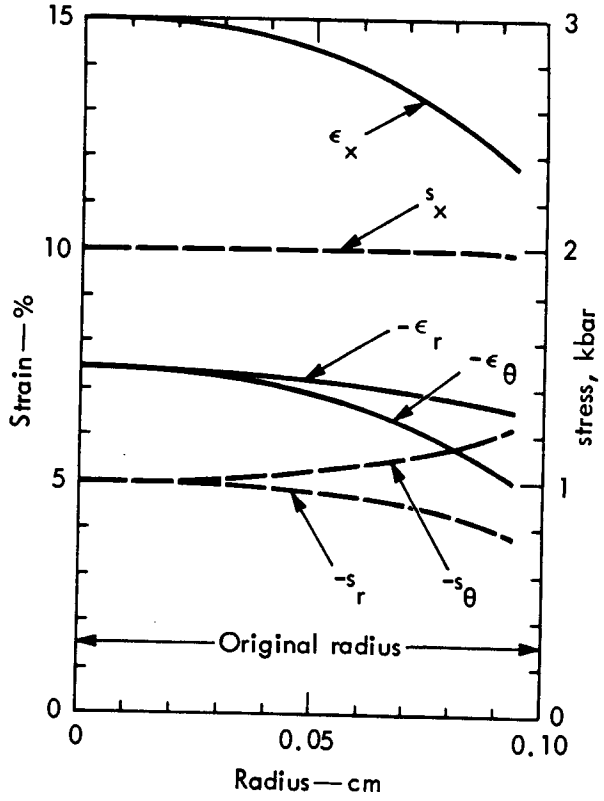

Fig. C3. Calculated distributions of components of total strain, ϵ_x, ϵ_r, and ϵ_θ, and corresponding stress deviators at rod midsection after elastic limit (Table CI t = 41). Stress and strain distributions are uniform below elastic limit.

at the outside boundary because the magnitude of s_r decreases. The flow adjusts itself so that the load on the midsection remains constant; i.e., the integral of the axial stress, σ_x, times the area of the cross section remains constant and equal to the value at the elastic limit. The result is that the pressure, P, assumes the quadratic dependence with radius seen in Fig. C4. Thus the dilation of the volume increases at the rod center and decreases at the rod exterior. In Fig. C3 it is seen that the elongation, ϵ_x, is greater at the rod center than it is at the exterior.

From the calculations, when the elongation measured at the outside of the specimen reaches $\epsilon_x = 0.12$, the value where rupture is observed experimentally, the intensity of plastic deformation at the interior of the specimen is $\gamma = 0.21$. The total stress in the interior at this time is $\sigma_x = 3.5$ kbar (Fig. C4).

Therefore, aluminum 6061-T6 will be considered to fail by rupture for $\gamma > 0.21$ and when a principal stress $\sigma > 3.5$ kbar. As pointed out above, the tension test does not examine the ultimate cohesive strength of a material because the boundary conditions do not permit the pressure component of stress to reach high tension values.

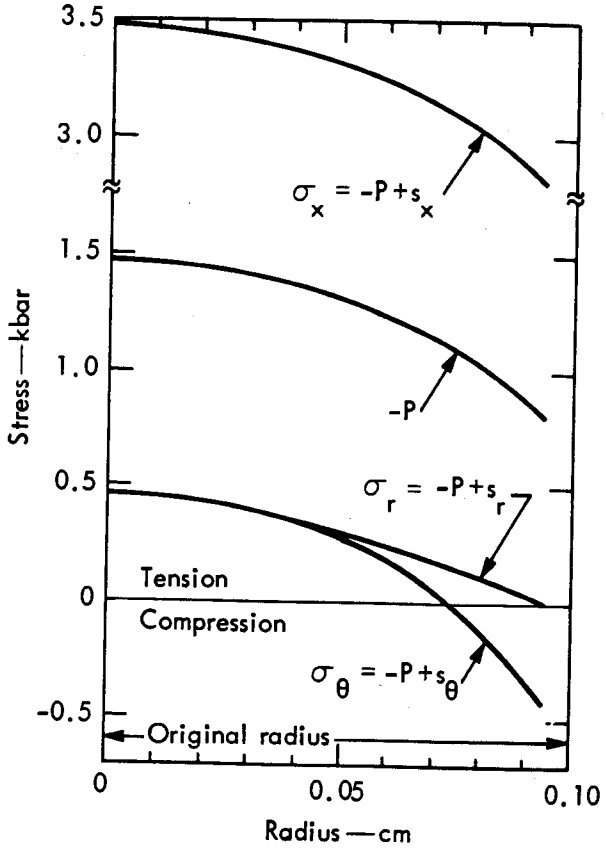

Fig. C4. Calculated distributions of stresses at rod midsection after elastic limit. Note: below elastic limit stress distribution is uniform.

The one-dimensional strain geometry used in spall experiments, however, does not have this limitation. The boundary conditions do not affect the stress magnitude that the pressure may attain. From previous experiments in one-dimensional strain geometry the spall strength of aluminum 6061-T6 is about 30-kbar tension. Therefore, the above rupture criteria can be supplemented with the condition that rupture also occurs for $P < -30$ kbar without affecting the results of the tension test calculation.

Distribution

LRL Internal Distribution

Michael M. May
C. Haussmann
C. Mc Donald
P. Archibald
C. Cline
P. Fleming
F. Johansen
J. O'Connor
N. Rawls
H. Rien
J. Routh
D. Sawle
R. Valentine
R. Landingham
R. Canan
H. Patton
S. Rhoads
W. Skinner
B. Weis
F. Eby
J. Lyle
G. Richards
C. Honodel
M. L. Wilkins
K. Hoge
P. Landon
C. Henry
W. Resemius
G. Carpluk
E. Kallemeyn
W. Gust
J. Rosengren
R. Batzel
G. Dorough
E. H. Fleming
A. Biehl

60

LRL Internal Distribution (Continued)

M. Loyd

J. Dittig

K. P. Ellis

W. S. Smith

K. E. Froeschner

TID File 30

External Distribution

E. D. Proudman, Jr.
P. R. Kosting
U. S. Army Materiel Command
Washington, D. C.

H. Markus
Frankford Arsenal
Philadelphia, Pennsylvania

E. V. Merritt
U. S. Army Aviation Materiel Laboratories
Fort Eustis, Virginia

L. Kasdorf
S. K. Cox
D. S. Malyevac
U. S. Naval Weapons Laboratory
Dahlgren, Virginia

J. Majowicz
Department of the Army
Washington, D. C.

T. J. Dawson
U. S. Naval Ship Engineering Center
Washington, D. C.

R. Eichelberger 3
Aberdeen Proving Ground
Aberdeen, Maryland

C. J. Skowronek
U. S. Naval Research Laboratory
Washington, D. C.

S. J. Kennedy 2
U. S. Army Natick Laboratories
Natick, Massachusetts

V. H. Pagano
U. S. Army Tank Automative Command
Warren, Michigan

A. R. Willner
Naval Ships Research and Development Center
Washington, D. C.

J. C. Pearson
G. Rugger
Picatinny Arsenal
Dover, New Jersey

R. E. Wittman
J. Hodges
Air Force Materials Laboratory
Wright-Patterson Air Force Base
Ohio

External Distribution (Continued)

E. N. Hegge
K. H. Abbott
A. L. Alesi
U. S. Army Material & Mechanics Research Center
Watertown, Massachusetts

Y. Nakamura
Aerojet General Corporation
Downey, California

R. E. Blair
U. S. Air Force Armament Laboratory
Eglin Air Force Base
Florida

P. H. Lynch
Rock Island Arsenal
Rock Island, Illinois

D. F. Phinney
U. S. Army Munitions Command
Dover, New Jersey

C. Bild
Sandia Corporporation
Albuquerque, New Mexico

T. Nicholas
H. Schwartz
Air Force Materials Laboratory
Wright-Patterson Air Force Base
Ohio

G. Maddux
Air Force Flight Dynamics Laboratory
Wright-Patterson Air Force Base
Ohio

J. Persh
Office of the Director of Defense Research and Engineering
Washington, D. C.

S. J. Lukasik
R. M. Thomson
F. W. Niedenfuhr
H. H. Test
Advanced Research Projects Agency
Washington, D. C.

G. Abrahamson/B. Ross
Stanford Research Institute
Menlo Park, California

E. P. Gains
Defense Atomic Support Agency
Livermore, California

J. Hansen
Norton Company
Worcester, Massachusetts

D. Trott
E. Bodine
Battelle Memorial Institute
Columbus, Ohio

External Distribution (Continued)

M. E. Backman
G. Hayes
R. A. Plauson
Naval Weapons Center
China Lake, California

D. J. Reid
D. Fylling
Food Machinery Corporation
San Jose, California

E. J. Janis
General Motors Technical Center
Warren, Michigan

C. S. Godfrey
Physics International Company
San Leandro, California

R. L. Bjork/H. E. Read
Shock Hydrodynamics Incorporated
Sherman Oaks, California

J. W. Taylor
Los Alamos Scientific Laboratory
Los Alamos, New Mexico

N. E. Chatterton
U. S. Air Force Armament Laboratory
Eglin Air Force Base, Florida

G. Duvall
Washington State University
Pullman, Washington

V. D. Frechette
Alfred University
Alfred, New York

J. J. Gilman
University of Illinois
Urbana, Illinois

P. S. Symonds
Brown University
Providence, Rhode Island

R. F. Recht
University of Denver
Denver, Colorado

R. T. Sedgwick
General Electric Space Sciences Laboratory
Philadelphia, Pennsylvania

J. M. Walsh
Systems Science and Software
La Jolla, California

S. Burstein
Courant Institute of Mathematical Sciences
New York, New York

C. R. Evans
Fort Halstead
Seven Oaks, Kent
United Kingdom

External Distribution (Continued)

J. Tillotsen
EG&G, Incorporated
Goleta, California

F. R. Fisher
National Academy of Sciences
Washington, D. C.

J. Berliez
Picatinney Arsenal
Dover, New Jersey

C. M. Glass
Aberdeen Proving Grounds
Aberdeen, Maryland

P. Kosting
U. S. Army Material Command
Washington, D. C.

W. Mannschreck
U. S. Naval Weapons Laboratory
Dahlgren, Virginia

J. J. Stiglich
Army Materials and Mechanics
Research Center
Watertown, Massachusetts

R. W. Pelz
R. V. Harrington
FERRO Corporation
Cleveland, Ohio

B. Bovarnich
Arthur D. Little Company
Cambridge, Massachusetts

R. Herman
Melpar, Incorporated
Falls Church, Virginia

Division of Technical Information Extension, Oak Ridge

WF/rt